Nuclear Structural Component Relevant Properties of Nickel-Based Alloys Produced via Additive Manufacturing

INL/RPT-24-80220
Revision 0

Advanced Materials and Manufacturing Technologies Program

M3CT-24IN1304021

AUGUST 2024

Asa Monson,
Michael Mulholland,
Tate Patterson, and
Michael McMurtrey

Idaho National Laboratory

Idaho National Laboratory

Battelle Energy Alliance manages INL for the U.S. Department of Energy's Office of Nuclear Energy

INL/RPT-24-80220
Revision 0

Nuclear Structural Component Relevant Properties of Nickel-Based Alloys Produced via Additive Manufacturing

M3CT-24IN1304021

Asa Monson,
Michael Mulholland,
Tate Patterson, and
Michael McMurtrey
Idaho National Laboratory

August 2024

Idaho National Laboratory
Idaho Falls, Idaho 83415

http://www.inl.gov

Prepared for the
U.S. Department of Energy
Office of Nuclear Energy
Under DOE Idaho Operations Office
Contract DE-AC07-05ID14517

Page intentionally left blank

ABSTRACT

Idaho National Laboratory initiated examination of nickel-based alloys manufactured via three different additive manufacturing methods for potential applications in nuclear, high temperature structural components. The three methods analyzed included laser powder bed fusion, blown powder laser directed energy deposition, and wire-fed gas metal arc directed energy deposition. With the rapid push towards additive manufacturing, codes do not exist that definitively define what is or is not tolerable for each process and application, such as with conventional, wrought products. This report contains the initial work to understand possible manufacturing methods for high temperature alloys, and specifically, void formation, microstructure evolution, corrosion, and mechanical properties. To generate mechanical test data, specimens were tested irrespective of voids and microstructures were analyzed to better understand how to negate/improve these issues. The preliminary results showed major decreases in mechanical performance for material tested. Test specimens will continue to be produced to further improve each additive manufacturing processes, quantify void acceptance, and better understand the most suitable high temperature alloys receptive to additive manufacturing and high temperature nuclear applications.

Page intentionally left blank

ACKNOWLEDGMENTS

This work was funded through the United States' Department of Energy's Office of Nuclear Energy's Advanced Materials and Manufacturing Technologies Program. The authors are grateful for the assistance with the technical work, including support from Qiufeng Yang with the molten salt testing, Ninad Mohale with the creep testing, Joel Simpson with the cyclic testing, and Robert Seifert and Mario Matos for assistance with the x-ray computed tomography.

Page intentionally left blank

CONTENTS

FIGURES

TABLES

Page intentionally left blank

ACRONYMS

AM	Additively Manufactured
CAD	Computer Aided Design
DED	Directed Energy Deposition
EBSD	Electron Backscatter Diffraction
EDS	Energy Dispersive X-ray Spectrometry
GMA-DED	Gas Metal Arc Directed Energy Deposition
INL	Idaho National Laboratory
IPF	Inverse Pole Figure
LPBF	Laser Powder Bed Fusion
LP-DED	Laser Powder Directed Energy Deposition
OES	Optical Emission Spectroscopy
ORNL	Oak Ridge National Laboratory
SEM	Scanning Electron Microscopy
STEM	Scanning Transmission Electron Microscopy
xCT	X-ray Computed Tomography

Page intentionally left blank

Nuclear Structural Component Relevant Properties of Nickel-Based Alloys Produced via Additive Manufacturing

M3CT-24IN1304021

1. INTRODUCTION

The Advanced Materials and Manufacturing Technologies (AMMT) Program is a Department of Energy, Office of Nuclear Energy program seeking to accelerate the development, qualification, demonstration, and deployment of advanced materials and manufacturing technologies. AMMT's overall goal is to enable reliable and economical nuclear energy. Currently, the AMMT Program is seeking to demonstrate accelerated qualification methods and develop a rapid qualification framework, using laser powder bed fusion (LPBF) Type 316H stainless steel as a demonstration case. LPBF of 316H will not address all nuclear structural needs, and there is interest in other alloys produced via advanced manufacturing techniques. In collaboration with Oak Ridge National Laboratory (ORNL), this work has sought to explore nickel-based alloys that are of interest to the nuclear community and determine printability and properties.

In previous work within the AMMT Program, three general categories were determined for nickel alloys use for nuclear structural systems: high temperature alloys, low cobalt alloys, and molten salt resistant alloys. [1] [2] One alloy was selected for further examination within high temperature alloys and low cobalt alloys. Molten salt resistant alloys were down selected to two alloys until preliminary corrosion results are attained. Haynes 282 was selected as the high temperature alloy, and Alloy 625 was chosen as the low cobalt alloy. The molten salt alloys included Hastelloy N and Haynes 244. The composition of Haynes 244 indicated a relatively high molten salt corrosion resistance though there was minimal supporting data. However, Haynes 244 has a better high temperature mechanical strength than Hastelloy N, and so it was of interest to determine if its molten salt performance was similar to Hastelloy N. Due to powder availability, and excellent high temperature mechanical properties, Haynes 282 was the primary focus this year.

Haynes 282 has a relatively high cobalt content of approximately 10 weight percent (wt%), which is not an ideal element to use within irradiation environments. Cobalt readily activates under neutron radiation, but it has superior high temperature strength when compared to other nickel alloys. Haynes 282 is a precipitation strengthened superalloy for high temperature structural applications including aerospace and land-based gas turbine industries. [3] Specifically, the titanium and aluminum content were controlled to balance the alloy strength and fabricability by maintaining a relatively low volume fraction of the gamma prime (γ') precipitate, i.e. $Ni_3(Ti/Al)$. The alloy was identified as a potential candidate for Advanced Ultra-Supercritical components such as a steam turbine disk (wrought) or a turbine valve body (cast), which led to an extensive study of the alloy's creep, fatigue and creep-fatigue performance [4] [5] [6], which lead to the approval of Haynes 282 in the ASME Boiler and Pressure Vessel Code in 2021 via Code Case 3024. [7]

Powder with a Haynes 282 composition is a commercial available product produced by several powder manufacturers A few research projects are exploring the use of LPBF 282 for the fabrication of high temperature supercritical CO_2 heat exchangers, [8] [9] but limited information has been reported regarding current applications. There are reports that indicated that high density, crack free LPBF 282 builds are possible [10] [11] [12], but there is limited work regarding high temperature mechanical properties for additively manufactured Haynes 282.

The as-printed microstructure has been found to consist of a cellular structure with textured grains elongated along the build direction [10] [11] [12] Lower yield and ultimate tensile strength and higher ductility have been reported for the as-printed LPBF 282 in comparison with wrought 282.with higher strength but lower ductility perpendicular to the build direction. [11] After conducting a full heat treatment with a solution annealing at 1150°C for 1 hour and the two-step aging treatment (2 hours at 1010°C followed by 8 hours at 788°C), the situation was reversed, with higher yield and ultimate tensile strength for the annealed LPBF 282 compared to wrought 282 but lower ductility. Shaikh et al. measured tensile properties at 800°C and reported similar strength for the annealed LPBF 282 and wrought 282, but higher ductility for the wrought alloy. [11] The standard solution annealing at 1150°C for 1hour does not result in the full recrystallization, as reported by Christofidou et al. [13] To achieve recrystallization, Boswell et al. solution annealed the LPBF 282 alloy for 1 hour at 1250°C, followed by a one-step aging treatment at 788°C for 8 hours. [12] Boswell et al. performed ten creep tests at 750°C, 410 MPa, and the ~80 hour lifetime was consistent with wrought 282 data. [12]. Shaikh et al. carried out creep testing at 927°C, 89MPa, and the lifetime was superior to the lifetime for wrought 282 along the build direction but inferior perpendicular to the build direction. [10] However, there is no publicly available data for fatigue performance or radiation effects for Haynes 282 in wrought nor additively manufactured forms.

This report covers the work performed at INL during fiscal year 2024, which has focused more on directed energy deposition (DED) methods for manufacturing AM Haynes 282 than LPBF. The primary focus has been on laser powder directed energy deposition (LP-DED), with preliminary work performed on wired-based gas metal arc directed energy deposition (GMA-DED). In addition to this, INL supported ORNL's work on LPBF with some mechanical testing on LPBF Haynes 282 provided by ORNL.

2. MATERIALS AND MANUFACTURING METHODS

2.1. Characterization Equipment

Material was heat-treated in a bottom loading box furnace, either to a solution annealed condition (1180 °C for 1 hour, followed by air cooling), or to a heat-treated with an aging treatment. A one step aging treatment was used on the solution annealed material (800 °C for 4 hours, followed by air cooling). Microstructure analyses were performed on polished (along the transverse and build direction) as-deposited, solution annealed, and age hardened samples using an FEI Quanta 650 scanning electron microscopy (SEM). The local crystal structure and orientation were determined utilizing electron backscatter diffraction (EBSD). Local composition analysis and elemental segregation was determined using energy dispersive X-ray spectrometry (EDS). Composition analysis on as-deposited samples was determined by Optical Emission Spectroscopy (OES). Size and composition of γ' precipitates in heat-treated samples were determined by scanning transmission electron microscopy (STEM) (ThermoFisher Spectra 300) analysis. The hardness of the as-deposited and heat-treated samples was measured according to ASTM E384 using a Vickers microindentation hardness testing system (LECO LM247AT) using a 300 g load with a 13 second dwell. The lattice parameter and crystal structure of the as-received powder, as-deposited, and heat-treated samples were examined using X-ray diffraction (Bruker D8 Advance) by Cu Kα radiation. The samples were inspected using θ-2θ from 20°-100° with a 0.02° step size. A VtomeX M300 180/300kV dual source with 100 µm pixel pitch detector x-ray computed tomography (xCT) system was used for non-destructive characterization and visualization of the voids in the AM material. xCT was performed on all specimens prior to mechanical testing. Creep testing was performed on dead weight loaded creep frames using a three-zone furnace for temperature control. Cyclic testing was performed on servo-hydraulic test frames, also utilizing a three-zone furnace for temperature control.

2.2. Laser Powder Bed Fusion

Haynes 282 powder was purchased, and the manufacturer's reported powder chemistry is shown in Table 1. A Renishaw 250 machine was used at the ORNL to optimize the Haynes 282 printing parameters

and fabricate large rods and blocks for microstructure and mechanical properties characterization. A hatch spacing of 86 μm, point spacing of 70 μm, and exposure time of 80 μs, were determined to be optimum for the processing of Haynes 282, with a laser power of 200 W and a powder layer thickness of 60 μm. [2]

Table 1. Manufacturer reported HY282 powder composition for LPBF and LP-DED builds.

Laser Powder Bed Fusion Powder Composition (weight percent, wt%)											
	Ni	**Cr**	**Co**	**Mo**	**Ti**	**Al**	**Fe**	**Mn**	**C**	**Si**	**O**
LPBF Alloy 282 Powder Composition	Bal.	19.37	10.24	8.33	2.11	1.54	-	-	0.05	0.03	0.01
LP-DED Alloy 282 Powder Composition	Bal.	16.92	9.35	8.23	1.95	1.52	0.22	0.02	-	-	-

The two large builds that were fabricated, one for ORNL and one for INL, and are displayed in Figure 1. Each of the rods and rectangular blocks were engraved to ensure the data that will be generated can be integrated into the digital manufacturing approach. The build configurations were based on the standard tensile/creep specimens at ORNL, and the standard tensile/creep and fatigue specimens at INL. The INL smooth button head fatigue specimen is 6” long, requiring rods 6” long and 0.75” in diameter or plates 6” long and 0.75” thick. A summary of all the samples and corresponding intended use is shown in Table 2.

Table 2. Sample blank specifications.

Build	Geometry	Dimention	Number	Testing	Engraving
ORNL	Cylindrical	0.5" dia, 4" long	10	Tensile along the BD	T1 to T10
ORNL	Cylindrical	0.5" dia, 4" long	10	Creep along the BD	C1 to C10
ORNL	Cylindrical	0.5" dia, 4" long	1	Microstructure char.	MC
ORNL	Rectangular	0.5"x5"x4"	1	Tensile per. To BD	HT1 to HT7
ORNL	Rectangular	0.5"x5"x4"	1	Creep per. To BD	HC1 to HC7
ORNL	Thin plates	0.5"x4"x(0.02", 0.04", 0.06" or 0.08")	3	TBD	1 to 3
INL	Cylindrical	0.5" dia, 6" long	8	Tensile along the BD	TV1 to TV10
INL	Cylindrical	0.5" dia, 6" long	8	Creep along the BD	CV1 to CV10
INL	Cylindrical	0.75" dia, 6" long	8	Fatigue along the BD	FV1 to FV8
INL	Rectangular	0.5"x6"x4"	1	Tensile per. BD	V sign
INL	Rectangular	0.5"x6"x4"	1	Creep per. BD	V sign
INL	Rectangular	0.75"x6"x6"	1	Fatigue per. BD	V sign

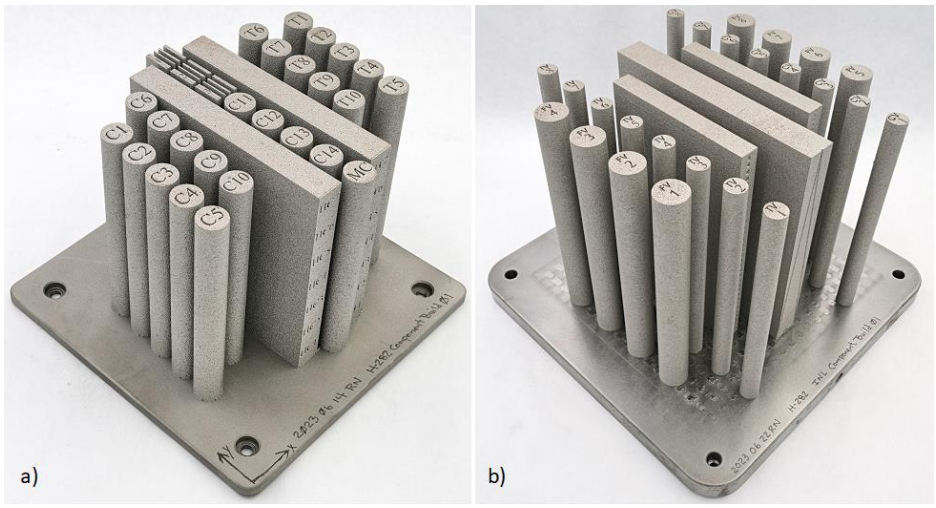

Figure 1. LPBF builds of mechanical test specimen blanks; a) ORNL build and b) INL build.

Creep specimens were machined from the CV and TV specimens and cyclic specimens (for fatigue and creep-fatigue testing) were machined from the FV cylinders. Portions of the cylinders were cross sectioned for optical and SEM to examine grain structure and defects.

2.3. Laser Powder Directed Energy Deposition

Laser powder directed energy deposition is an additive manufacturing process developed for a wide range of applications. LP-DED is a solid freeform manufacturing technique that transforms metallic powders into dense three-dimensional parts from a CAD model, following the process described in Figure 2.

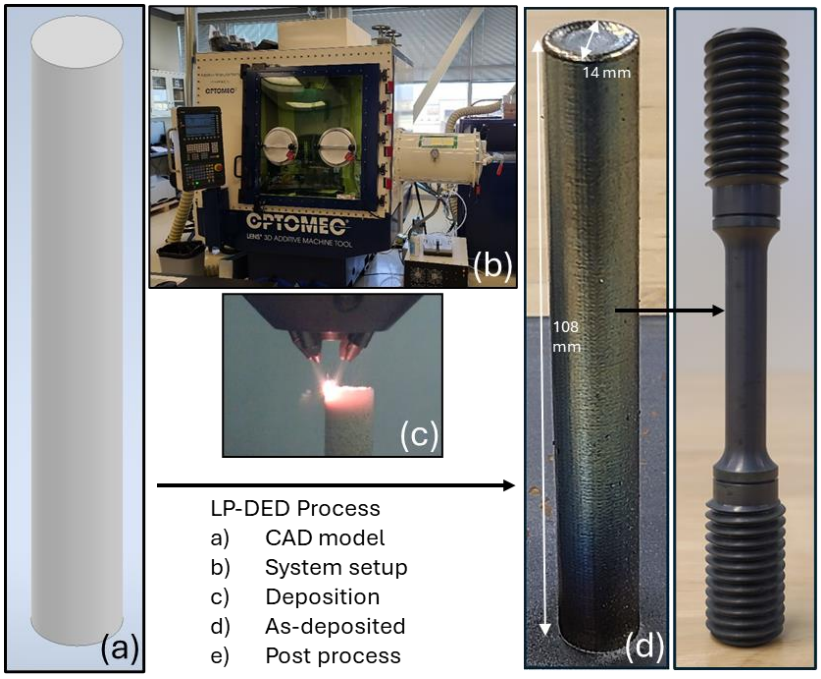

Figure 2. LP-DED Process Flow. (a) Part is developed as a CAD model, (b) the model is sliced, and G-code/M-code is created, (c) part is fabricated using blown powder deposition, (d) the as-deposited part then goes into (e) post processing involving heat treatment and machining.

Commercially supplied, gas atomized HY282 powder was used for this work. The powder has a composition as shown in Table 1, measured by optical emission spectroscopy (OES) with a particle size distribution of 45-105 μm in diameter. The substrate was a 6" x 6" x 0.5" 1020 steel plate. During the LP-DED process key parameters including laser power, powder feed rate, and deposition rate influence the final microstructure and mechanical properties. These parameters were selected based on initial test prints to reduce the number of voids. The process parameters, laser power (300 W), powder feed rate (9.5 g/min), deposition rate (9.3 mm/s), hatch spacing (0.381 mm), hatch angle (67°), and layer thickness (0.127 mm) were used to fabricate cylinders with dimensions 108 mm x 14 mm.

The system utilized in this work was an Optomec MTS 500 which uses a laser to melt metallic powder fed through four nozzles towards the focal plane of the laser beam. The system uses a 1070 nm wavelength, 1 kW YLR laser from IPG Photonics with a focused beam diameter of 0.6 mm. The samples were deposited in an argon environment by evacuating to a pressure of 4.5 torr and backfilling with 99.9% purity argon. Argon gas with the same purity was also used as a shielding gas and the powder carrier gas. Hardness measurements were taken on the as-deposited, solution annealed, and aged material. The final hardness values were calculated by averaging the 80 indentations arranged in an 8x10 matrix with a spacing of 500 μm.

2.4. Wire-based Gas Metal Arc - Directed Energy Deposition (GMA-DED)

Gas metal arc – directed energy deposition (GMA-DED) uses the gas metal arc welding (GMAW) process to deposit material in a layer-by-layer method. This work used a six-axis robot and welding power supply with a push-pull wire feed configuration capable of the short circuit welding mode known as cold metal transfer. The composition for the nominal 0.045-inch (1.1 mm) diameter solid wire filler metal (or feedstock) is shown in Table 3, and the filler metal conformed to the American Welding Society specification AWS 5.14: 2024 *Specification for Nickel and Nickel-Alloy Bare Welding Electrodes and Rods* [14] based on a ERNiCrCoMo-2 filler metal.

Table 3. Manufacturer reported Haynes 282 filler metal composition for GMA-DED builds.

GMA-DED Filler Metal Composition (wt%)							
Ni	**Cr**	**Co**	**Mo**	**Ti**	**Al**	**Fe**	**W**
Bal.	19.6	10.28	8.5	2.2	1.46	0.9	0.1
Nb	**Ta**	**Mn**	**C**	**Si**	**P**	**S**	**B**
0.11	<0.01	0.1	0.06	0.05	0.003	<0.002	0.004

The block that was built was approximately 150 mm tall, 100 mm long, and 50 mm wide, and the dimensions were solely created for easy extraction of specimens for creep and low cycle fatigue/creep-fatigue testing. A photo of the completed deposit is shown in Figure 3. The block consisted of eight weld beads wide and 70 layers tall. The average current, voltage, travel speed, and wire feed speed values were 130 A, 17 V, 4 mm/s, and 86 mm/s, respectively. The shielding gas was a 98% argon – 2% hydrogen mix with a flow rate of 15.0 L/min. The interpass temperatures were not measured nor maintained. For consistent heat input for each weld bead, parameters were not adjusted for the weld start (left of photo in Figure 3) and the weld end (right of photo in Figure 3). However, this created "cold" starts and "hot" ends

due to non-uniform temperatures in these regions. For future testing, specimens were only extracted from the center, steady-state region of the block.

Figure 3. Photo of the robotic welding setup for wire arc additive (left) and the completed GMA-DED block (right).

3. RESULTS

3.1. Laser Powder Bed Fusion

3.1.1. Optical Characterization

Cylinder FV1 was solution annealed and cross sectioned for microstructural analysis. Previous INL heat treatments on samples provided by EOS to optimize solutionizing treatment ended with a furnace cool rather than an air cool. [1] After heat treatment, a piece was cut from the bottom end (near build plate) of FV1 for microstructural analysis. Examination with the optical microscope revealed significant porosity, as shown in Figure 4. The Keyence Image Analysis software was used to quantify the porosity.

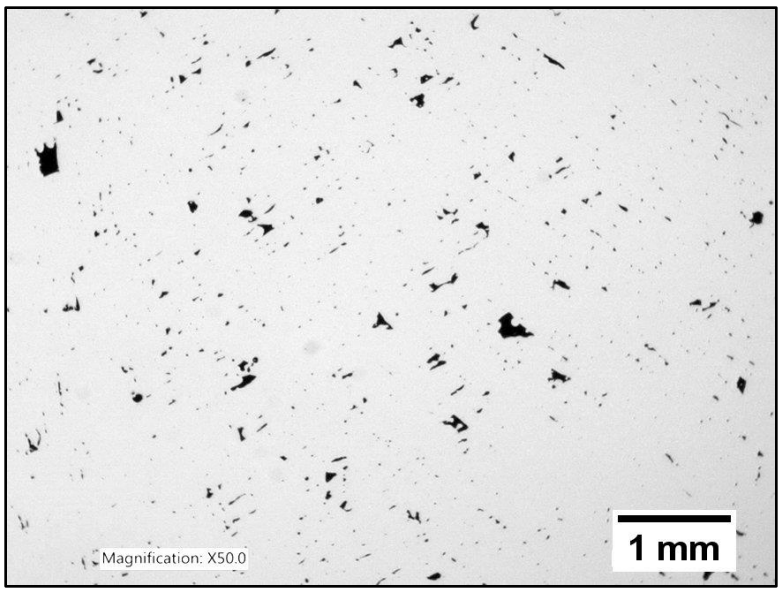

Figure 4. Optical micrograph of porosity near bottom of FV1. 50x magnification.

The porosity near the bottom was measured to be ~2 area %. FV1 was then serial sectioned to study the variation in porosity throughout the sample height and the porosity extended throughout the sample. The center slice was mounted and polished to quantify the porosity, which is shown in Figure 5. The porosity was measured to be ~5%. Tensile blank TV4 was also sectioned near the build plate to check for porosity. This sample also had porosity, but significantly less than FV1, as seen in Figure 6. The porosity was measured to be 0.7%. The results are summarized in Table 4. FV5-8 are better than FV1, but still have significant porosity. FV6 has the lowest porosity. A section from the EOS samples was also examined for porosity. The EOS sample has much lower porosity than the ORNL samples, as seen in Table 4.

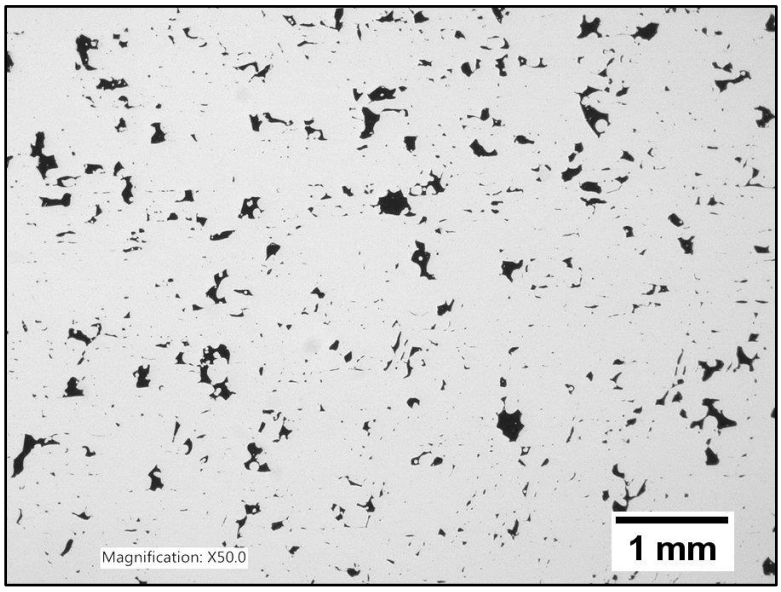

Figure 5. Optical micrograph of porosity in center slice of FV1. 50x magnification.

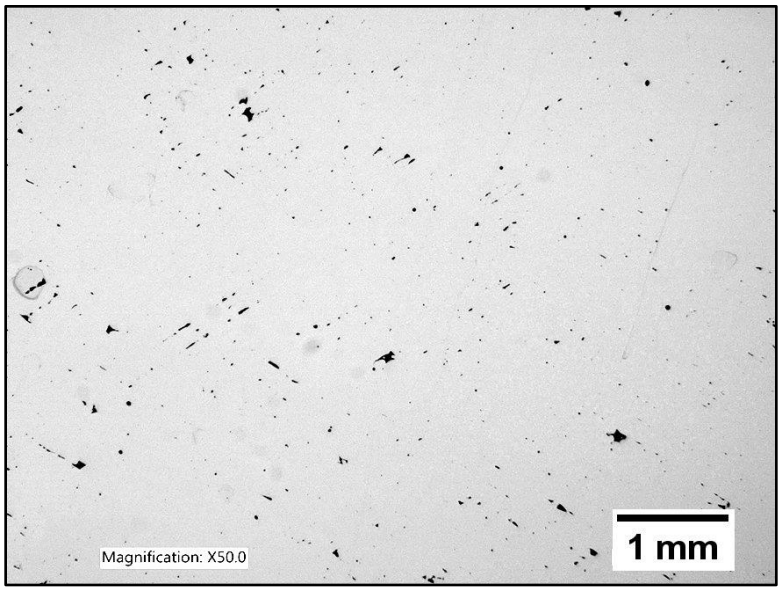

Figure 6. Optical micrograph of porosity near bottom of TV4. 50x magnification.

Table 4. Porosity measurements.

Sample	Porosity (area %)
TV4, 4 mm end	0.67
FV1, slice 6, bottom	1.95
FV1, center slice	4.76
FV5, bottom	0.79
FV6, top	0.59
FV7, bottom	0.27
FV8, top	1.07
EOS 1100 1h	0.05

3.1.2. SEM Characterization and heat treatment study

To investigate the effectiveness of the heat treatments in recrystallizing the microstructure through thickness, a piece of sample FV1 was reheated to 1180 °C for 1 hour and then air cooled. Scans were taken from the center of the cross section in three different locations. Figure 7 shows an inverse pole figure (IPF) map of the center-most location. At the magnification of the scan, it was not possible to avoid the copious porosity, so several pores are visible. The map reveals mostly equiaxed grains, indicating that the sample was mostly recrystallized even in the center. Some non-recrystallized regions are still present. There were regions of small grains found next to the large pores. This is present in several of the scans, such as the scan shown in Figure 8. It suggests that either the regions near the pores recrystallized later than the interior regions, or grain size was restricted near the pores for another reason.

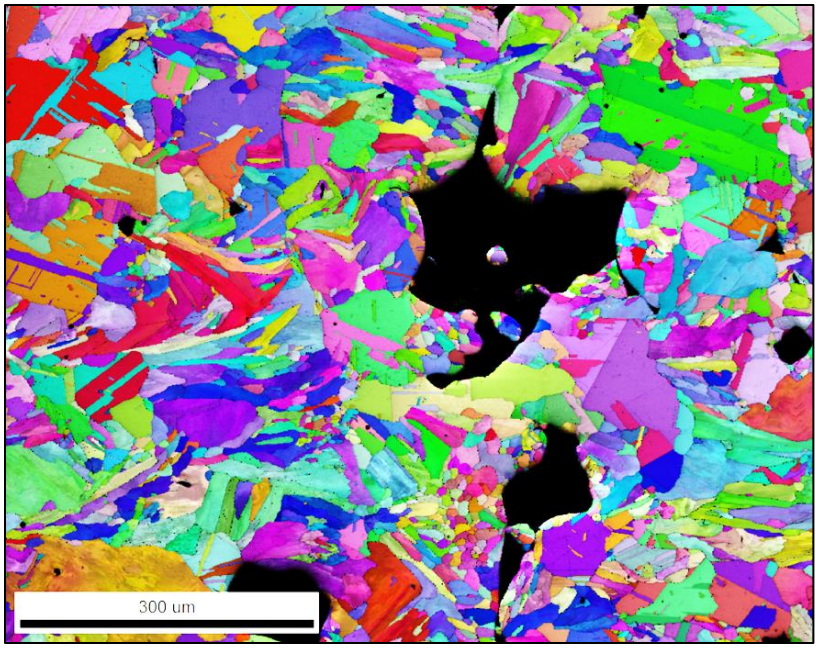

Figure 7. IPF map from center of sample FV1 heat treated at 1180 °C for 1 hour.

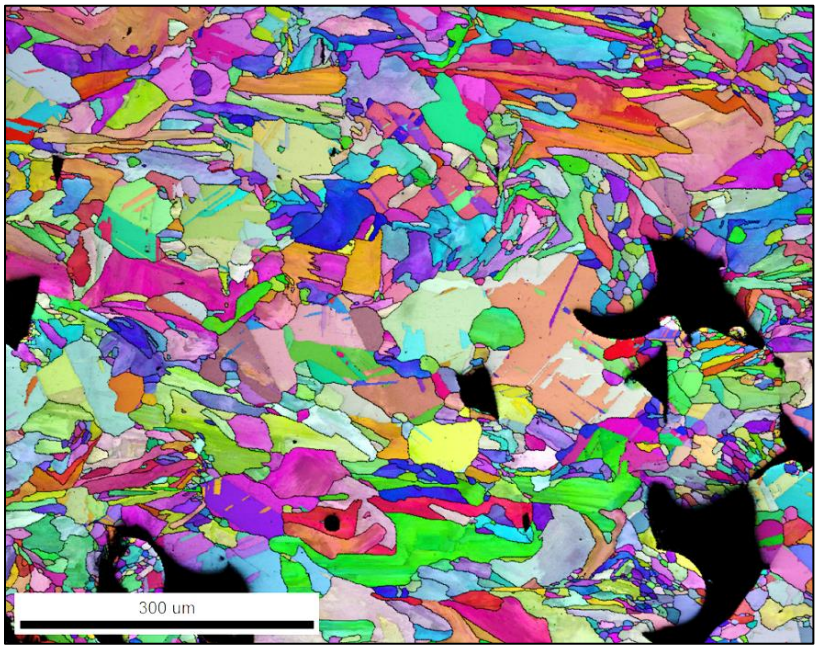

Figure 8. IPF map from a region 6 mm away in the radial direction from the previous map of specimen FV1 heat treated at 1180°C for 1 hour.

The earlier EOS samples were furnace cooled after solution annealing at 1180 °C for 1 hour. Comparison of Figure 7 and Figure 8 with Figure 9 shows a smaller grain size for the air-cooled FV1 sample. Table 5 presents a comparison of the measured grain sizes of the EOS samples and the ORNL material.

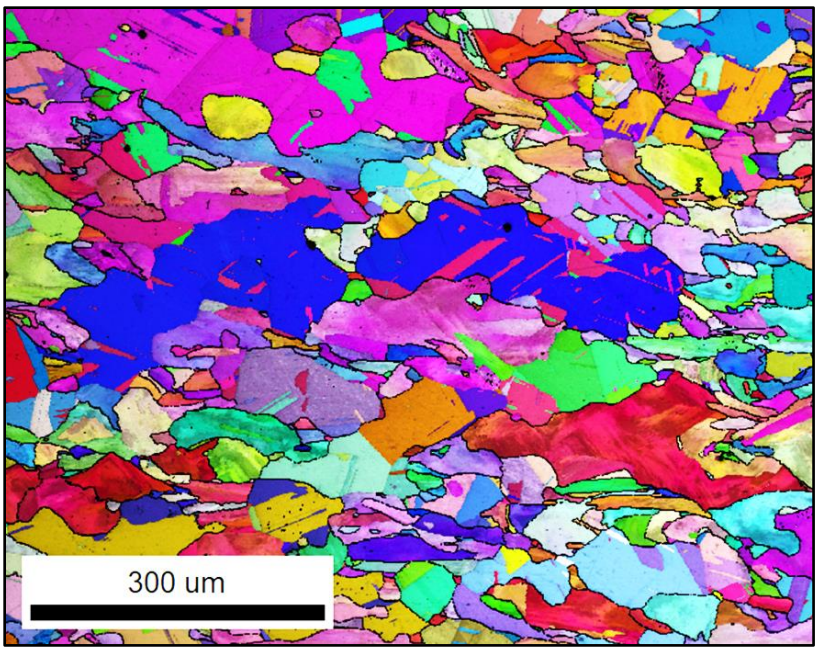

Figure 9. EBSD IPF map of LPBF Haynes 282 EOS sample heat treated at 1180°C for 1 hour and furnace cooled.

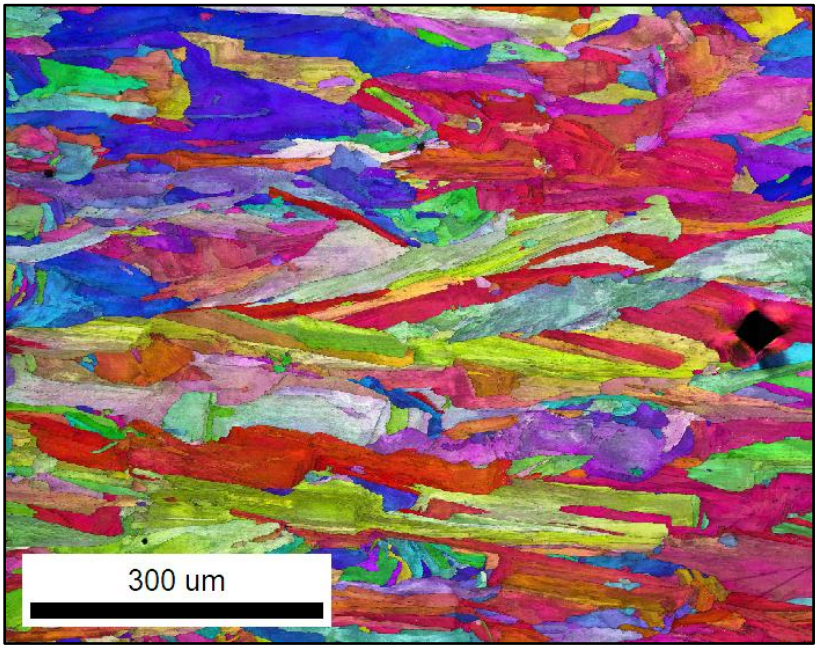

Figure 10. EBSD IPF map of LPBF Haynes 282 EOS sample heat treated at 1180°C for 0.5 hour and furnace cooled.

During the EOS sample heat treatment study performed at INL, it appeared that the grain growth occurred rapidly after recrystallization, as seen by the difference in recrystallization state between specimens annealed at 1180 °C for 0.5 hour vs. 1180 °C for 1 hour: Samples annealed at 1180 °C for 0.5 hour were mostly un-recrystallized (as seen in Figure 10), while samples annealed at 1180 °C for 1 h were mostly recrystallized with a grain size of 112 µm. The microstructure is quite sensitive to time at 1180 °C.

This explains the difference observed in the slower furnace cool vs. air cool after heat treatment, as described below.

Table 5. Average grain size of LPBF Haynes 282 samples under various aging conditions.

Manufacturer	Sample	Condition	Area weighted average grain size (microns)
EOS	1	as printed	88
		1250 1 h	255
		1250 2 h	282
		1210- 2 h	327
		1180 1 h	112
		1180 0.5 h	Mostly unrecrystallized
		1160 1 h	Mostly unrecrystallized
ORNL	FV1	1180 1 h	55
	TV1	1180 1 minute+ 1 h	141 in BD, 108 in TD
	TV1	1180 1 minute+ 1 h + 800 4 h	143
	CV3	1180 1 h	77

When aging the remainder of the tensile and fatigue samples, a mistake in the programming of the furnace was made. The samples were consequently subjected to 1180 °C for 1 minute, followed by forced air cooling. When this was realized, the samples were again reheated to 1180 °C and held for 1 hour, followed by air cooling. The grain size of the sample TV1 was studied to understand the implication of the mistake. Figure 11 shows an IPF map from an EBSD scan from the center of TV1. As seen in the figure and in Table 5, the grain size of TV1 after the deviant heat treatment is 141 μm, which is larger than that of FV1 and also slightly larger than the EOS sample that was aged at 1180 °C for 1 h and furnace cooled. This indicates that the time that TV1 spent at close to the critical recrystallization temperature (most likely during the double heatup) is more similar to the EOS sample time (which includes heat up and furnace cooling), than FV1 which had a single heat up and then rapid air cooling. The recrystallization had enough time to initiate during each heat up phase of the double heat treatment, even though the sample only spent 1 minute at 1180 °C for the first heat treatment. It is also interesting that the grain size of sample TV1 in the transverse direction is 108 μm, which indicates an isotropic grain size, probably a remnant of the initial highly anisotropic microstructure. The grain size of creep sample CV3 was also checked. This sample received a heat treatment of 1180 C for 1 h followed by an air cool. The grain size in this case was 77 microns, which is close to that of FV1.

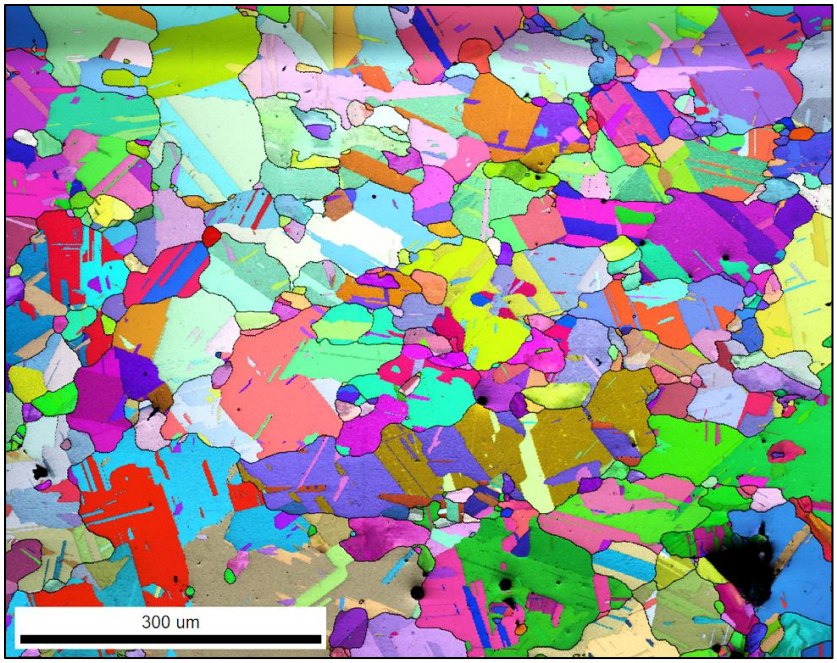

Figure 11. IPF map of center of sample TV1.

The sample that received the double heat treatment at 1180 °C was then aged at 800 °C for 4 h to precipitate gamma prime. The grain size was again checked by EBSD, and is 143 μm, which is essentially the same as the solution treated sample. This is expected due to the low temperature and since gamma prime and carbide precipitation at 800 °C should pin the grain boundaries and prevent any significant grain growth.

3.1.3. X-Ray Computed Tomography Characterization

xCT was performed on all creep and cyclic specimens prior to testing, with examples shown in Figure 12 through Figure 24. For each example, three cross sectional images are shown, two taking longitudinally, one circumferentially, and one "through thickness" is shown to demonstrate the void density through a volume of the specimen. While these do not give the entirety of the data collected during the xCT scan, it does provide a representative example of the structure of the specimens. Of the creep specimens, significant defects were seen in TV-1, CV-4 and CV-5 had relatively few defects, and the rest were in between with some moderate level of defects. FV-2, FV-3, and FV-4 had a noticeably higher void density than the other fatigue specimens.

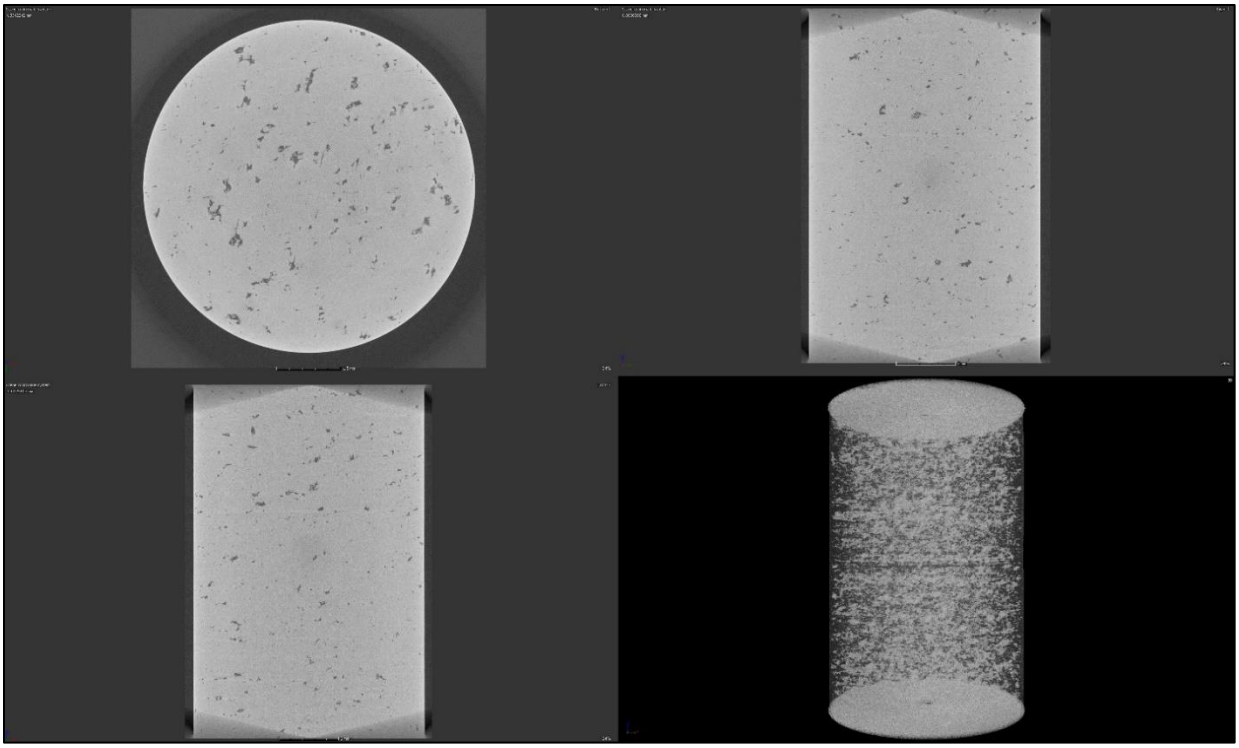

Figure 12. Example cross sections and full volume section (lower right) from the xCT scans of specimen TV-1.

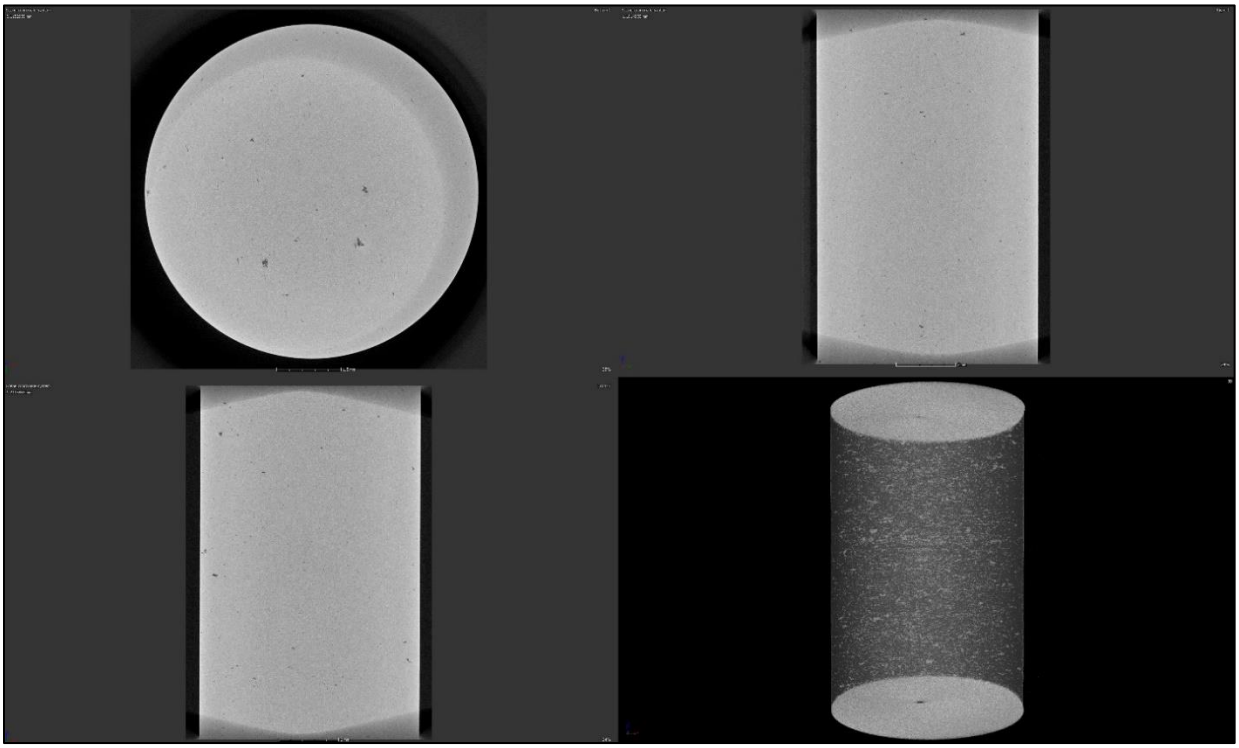

Figure 13. Example cross sections and full volume section (lower right) from the xCT scans of specimen TV-4.

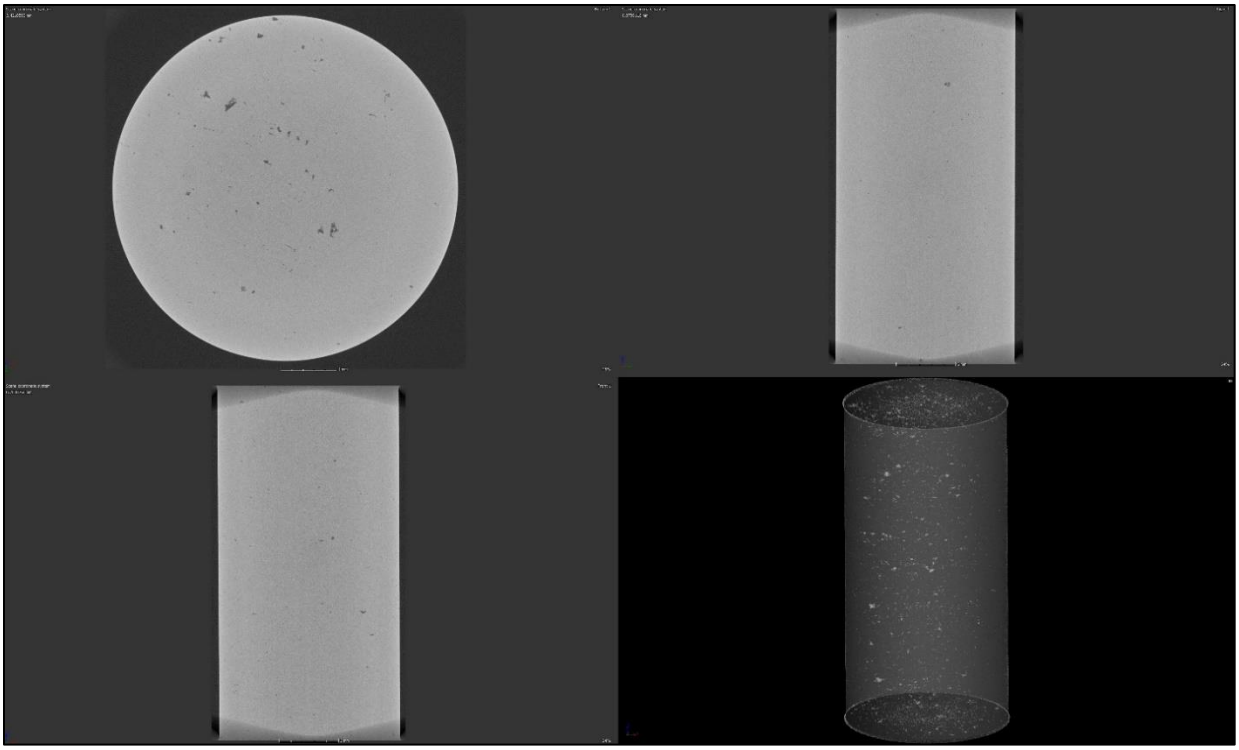

Figure 14. Example cross sections and full volume section (lower right) from the xCT scans of specimen CV-2.

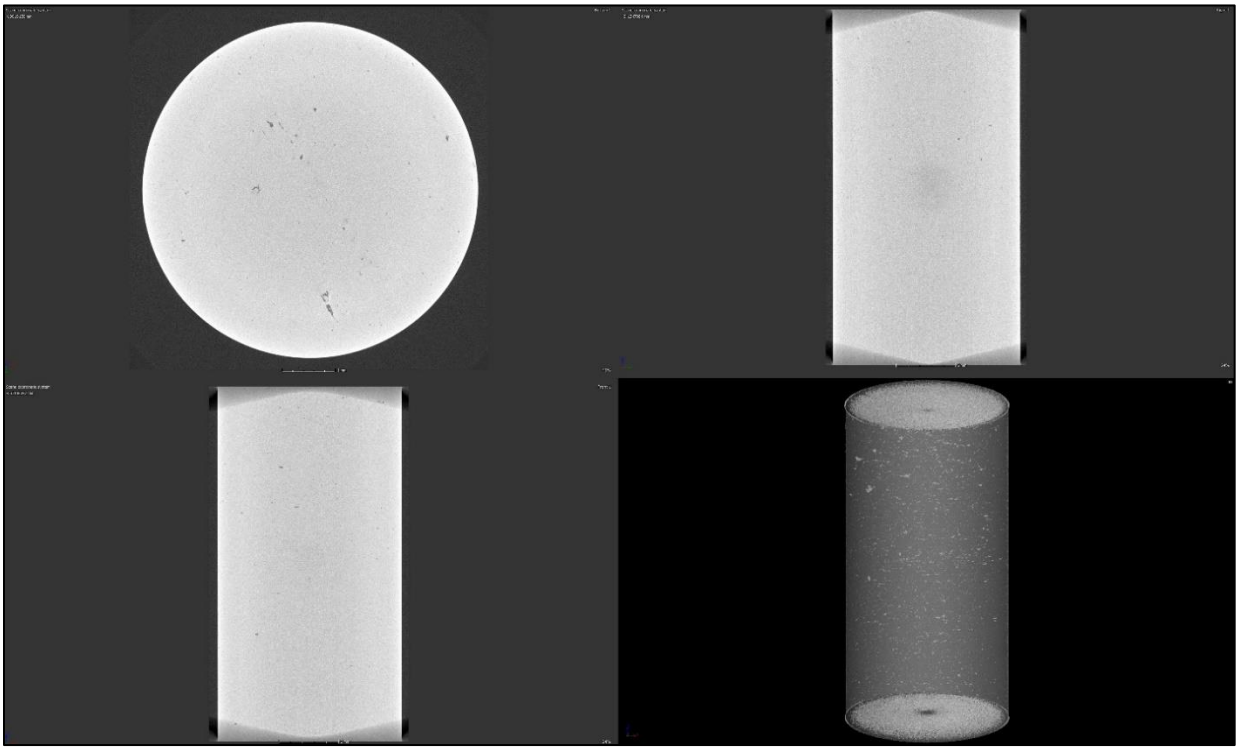

Figure 15. Example cross sections and full volume section (lower right) from the xCT scans of specimen CV-3.

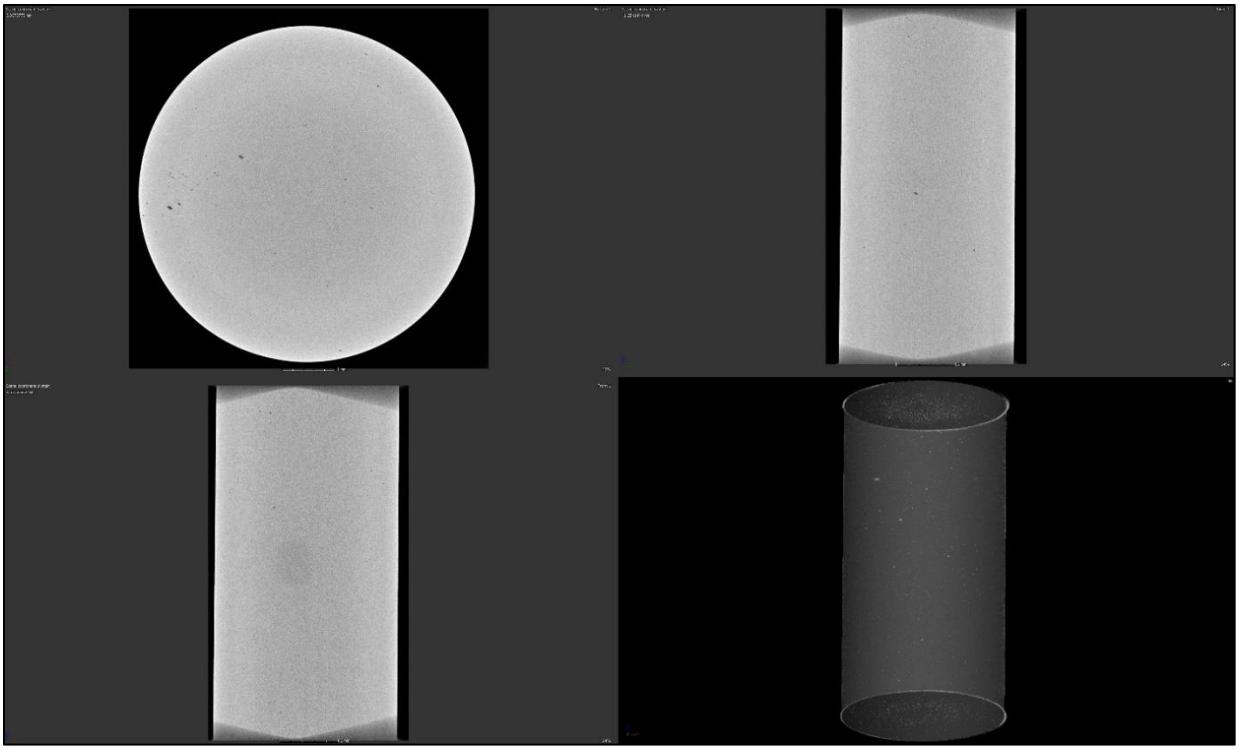

Figure 16. Example cross sections and full volume section (lower right) from the xCT scans of specimen CV-4.

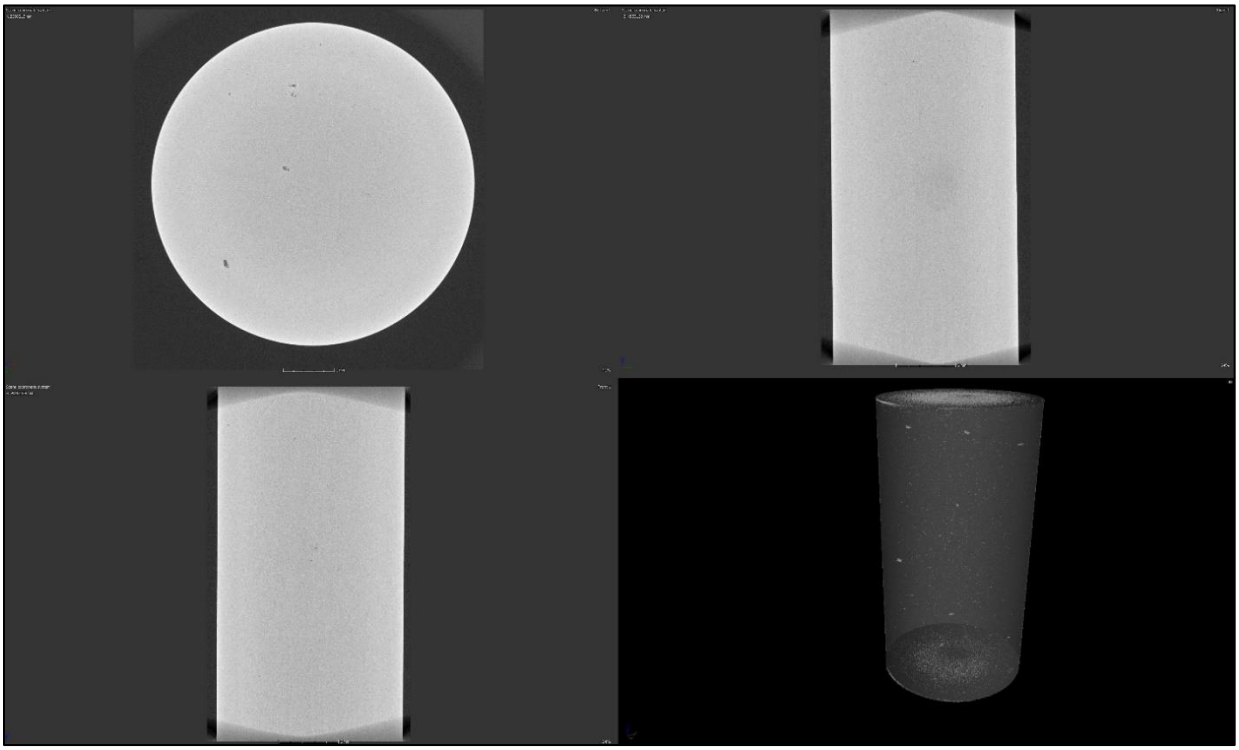

Figure 17. Example cross sections and full volume section (lower right) from the xCT scans of specimen CV-5.

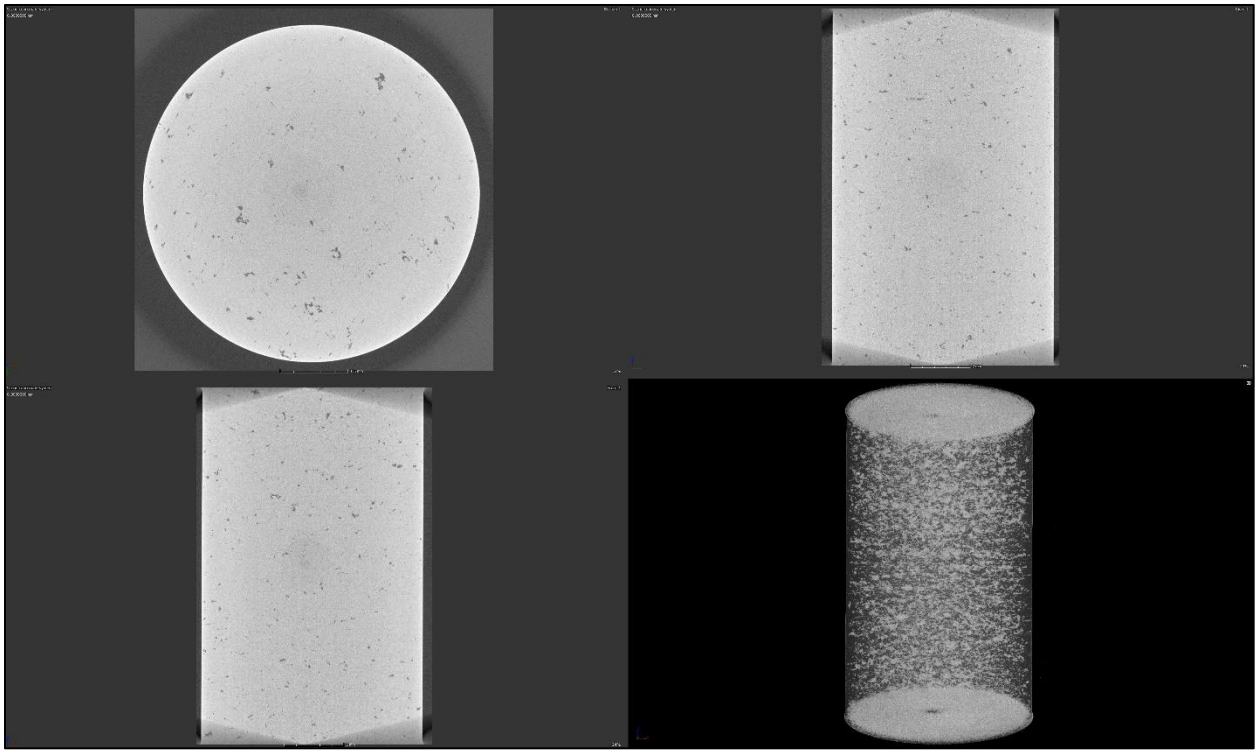

Figure 18. Example cross sections and full volume section (lower right) from the xCT scans of specimen FV-2.

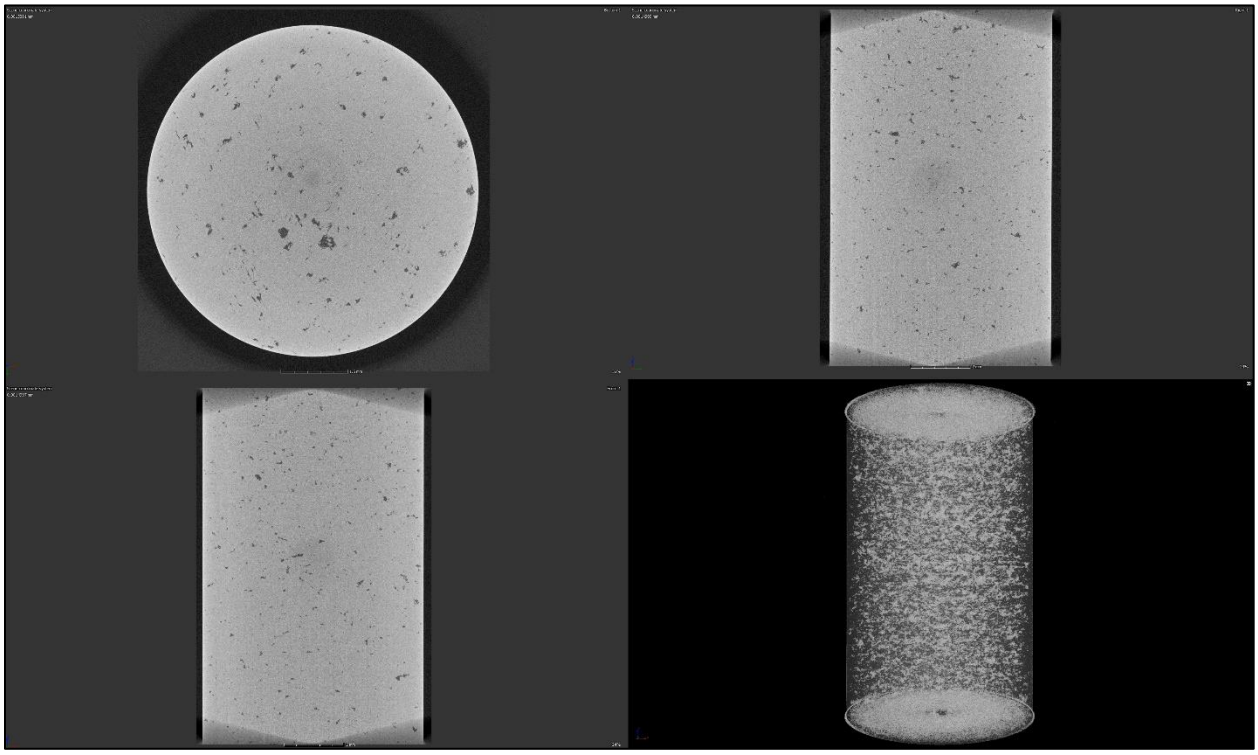

Figure 19. Example cross sections and full volume section (lower right) from the xCT scans of specimen FV-3.

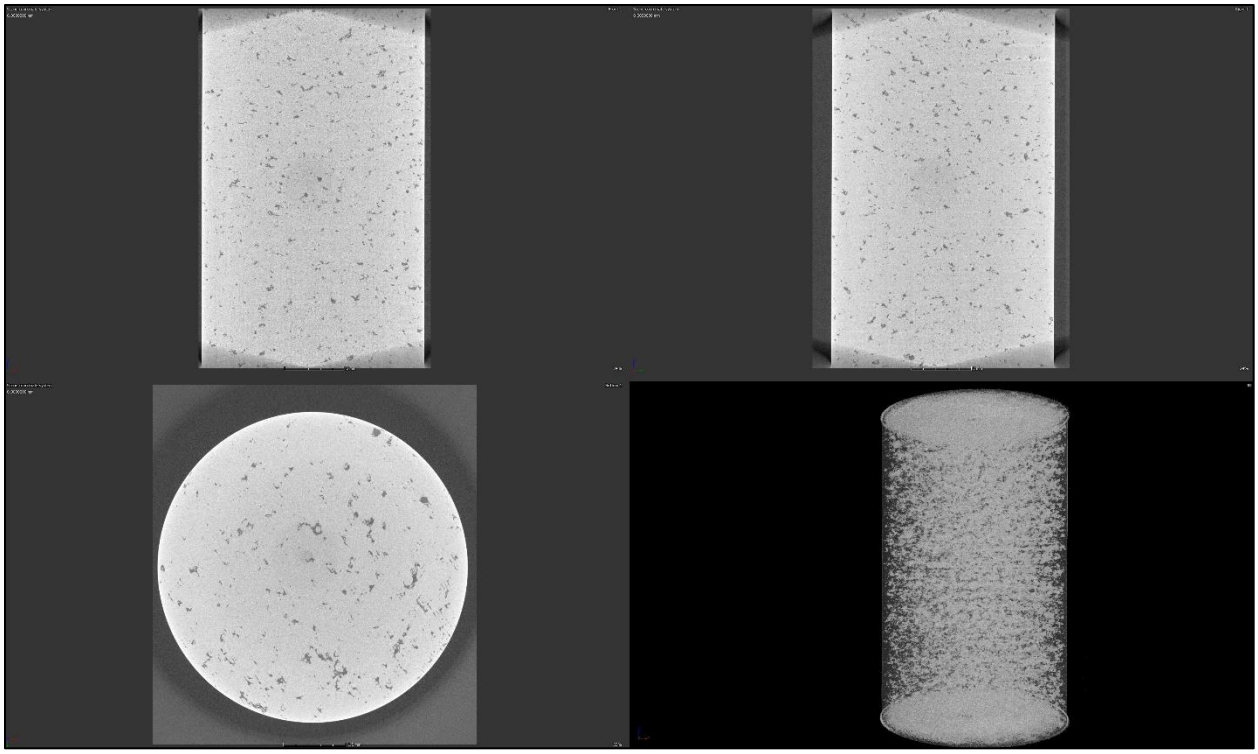

Figure 20. Example cross sections and full volume section (lower right) from the xCT scans of specimen FV-4.

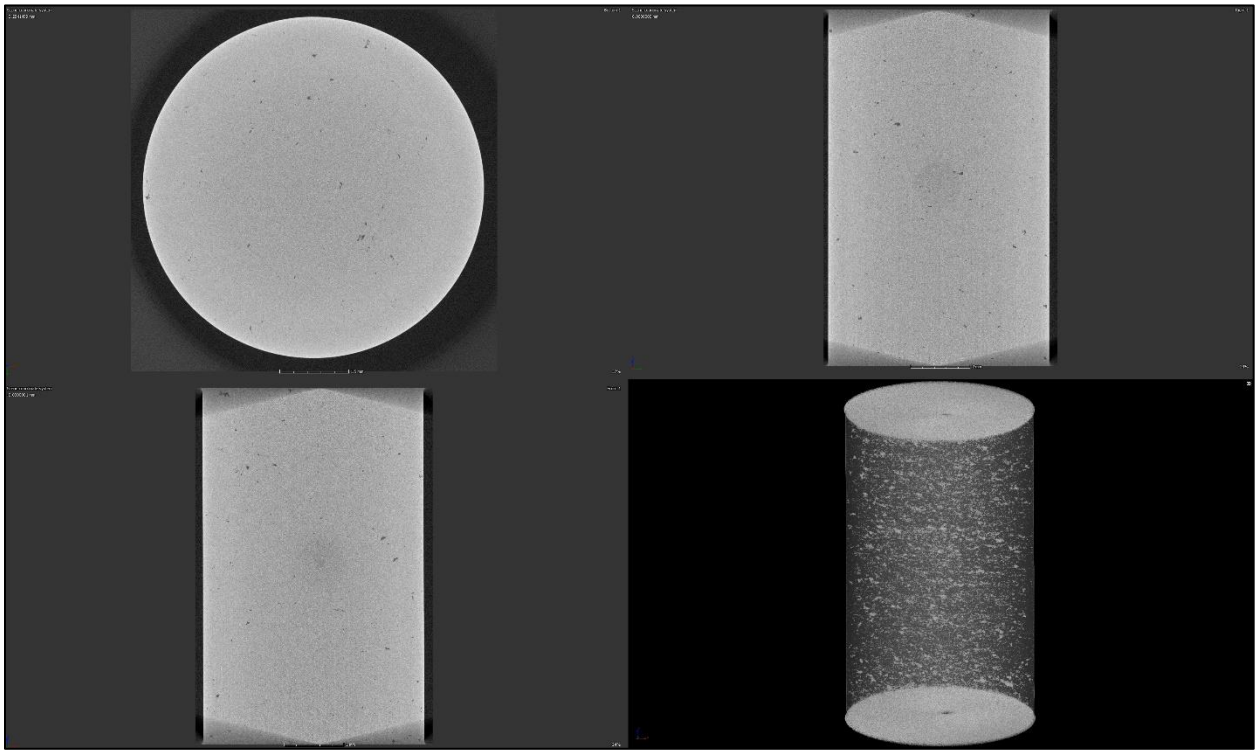

Figure 21. Example cross sections and full volume section (lower right) from the xCT scans of specimen FV-5.

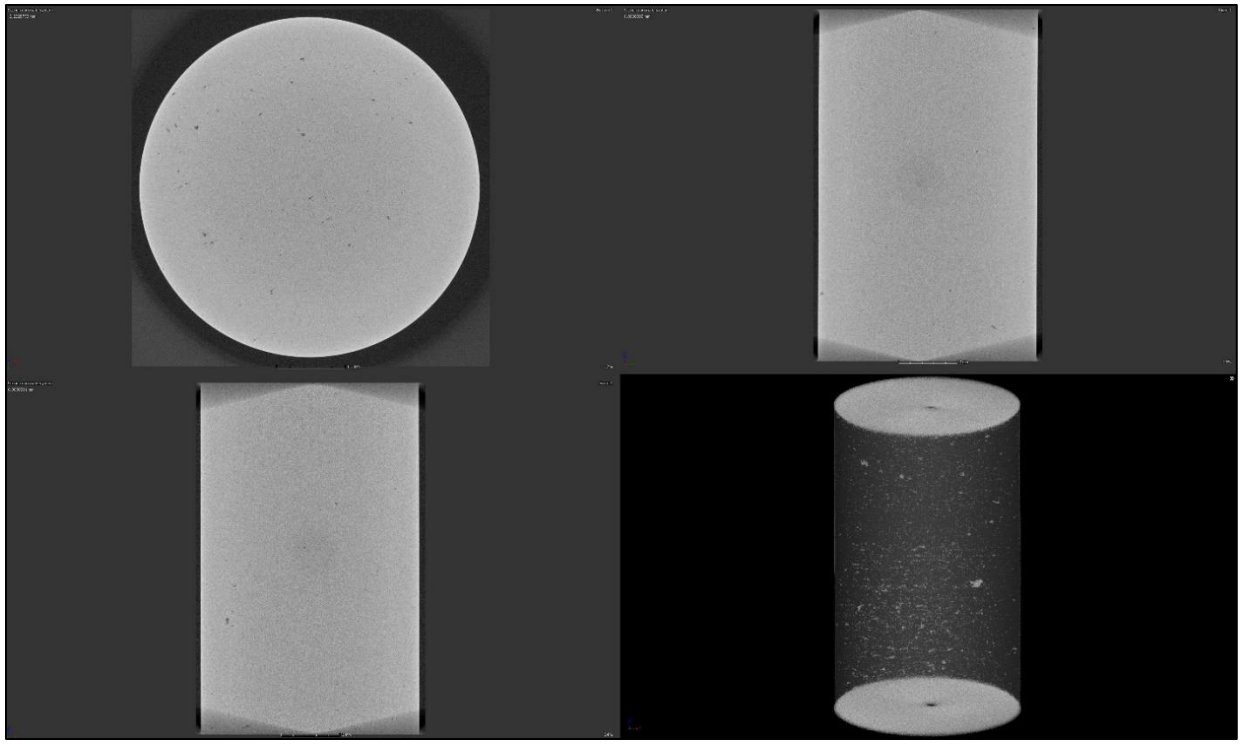

Figure 22. Example cross sections and full volume section (lower right) from the xCT scans of specimen FV-6.

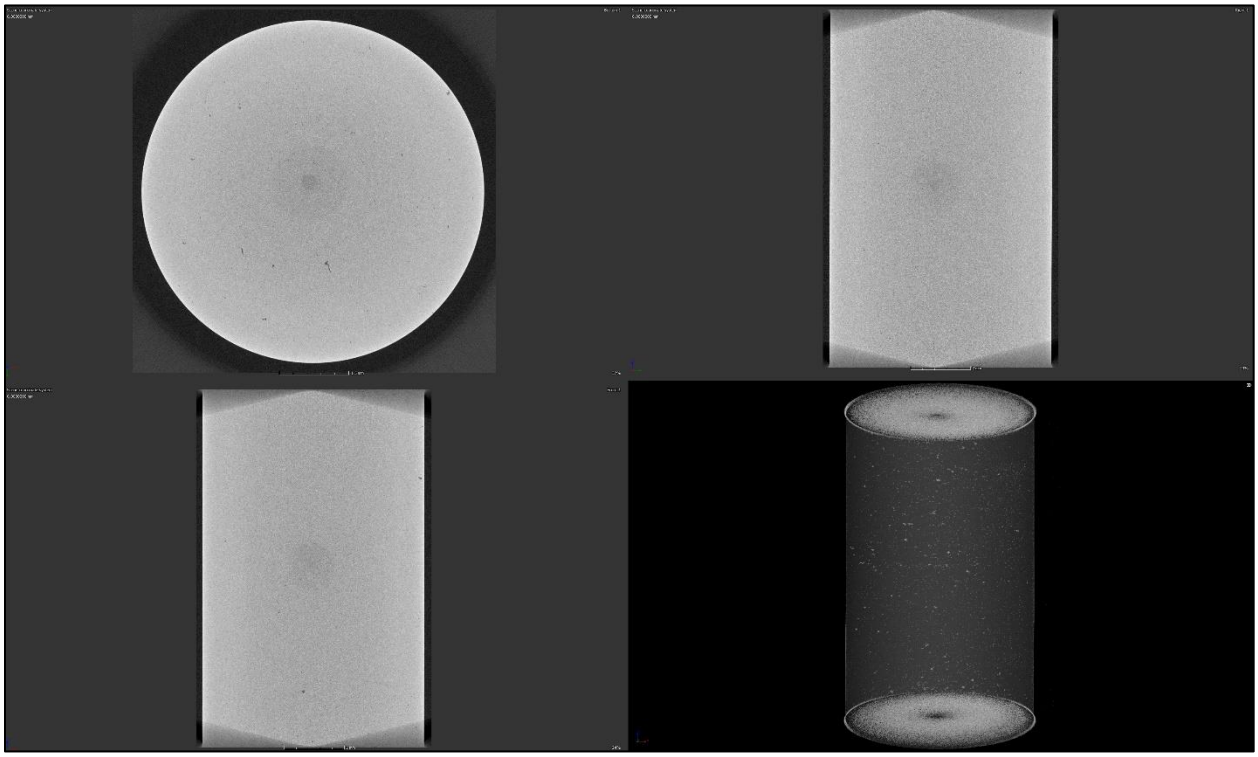

Figure 23. Example cross sections and full volume section (lower right) from the xCT scans of specimen FV-7.

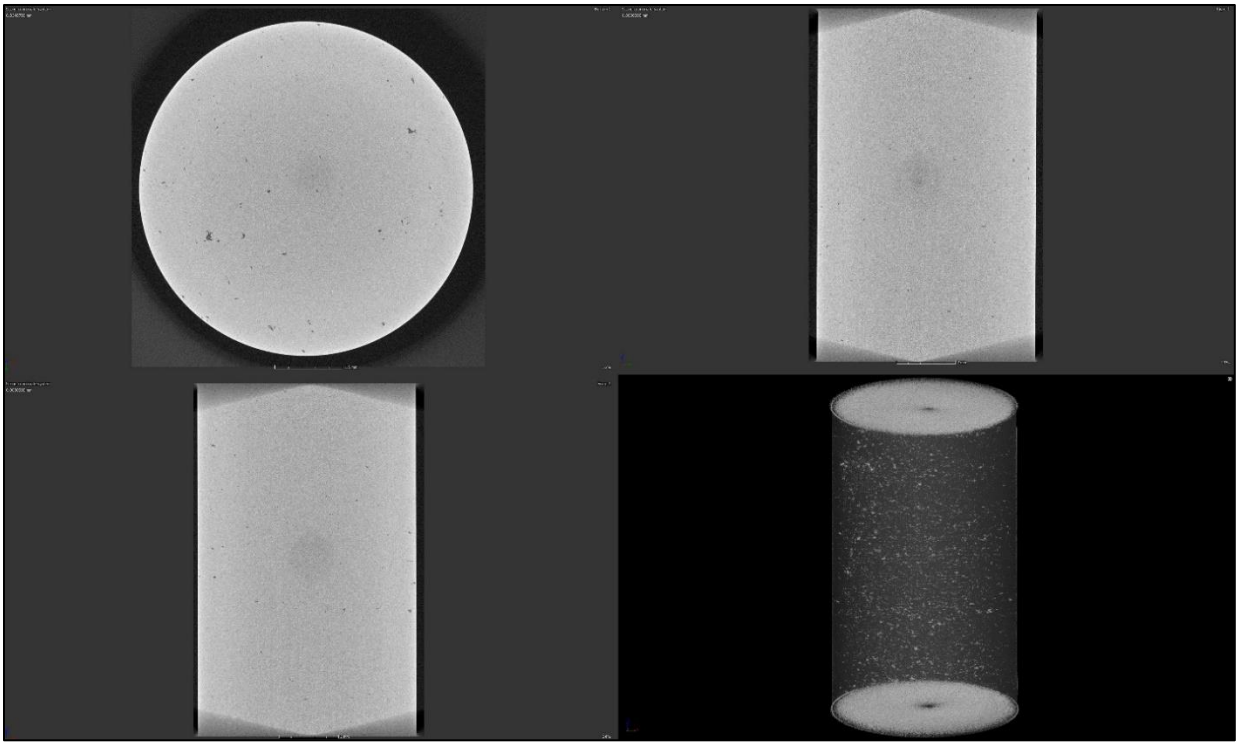

Figure 24. Example cross sections and full volume section (lower right) from the xCT scans of specimen FV-8.

3.1.4. Creep testing

Creep testing was all performed at 750 °C. Three different stress levels were used to test different conditions. 300 and 350 MPa were chosen to match similar tests being performed on different builds of LPBF Haynes 282 at ORNL. 320 MPa was chosen to compare to past testing of wrought Haynes 282 performed at INL as part of a concentrating solar power program that was examining potential receiver materials, which included Haynes 282. [15] In general, ductility was quite low for each of the LPBF specimens, though particularly for TV-1, as seen in the creep curves found in Figure 25. When compared to wrought material in Figure 26, the rupture life was also quite short, with the LPBF material rupturing at about 220 hours, while the wrought ruptured around 1,400 hours. While some variation in creep data is expected, a factor of 7 goes beyond that and indicates issues with the LPBF material. Final elongation was determined by measuring the specimens directly after testing and the results are summarized in Table 6.

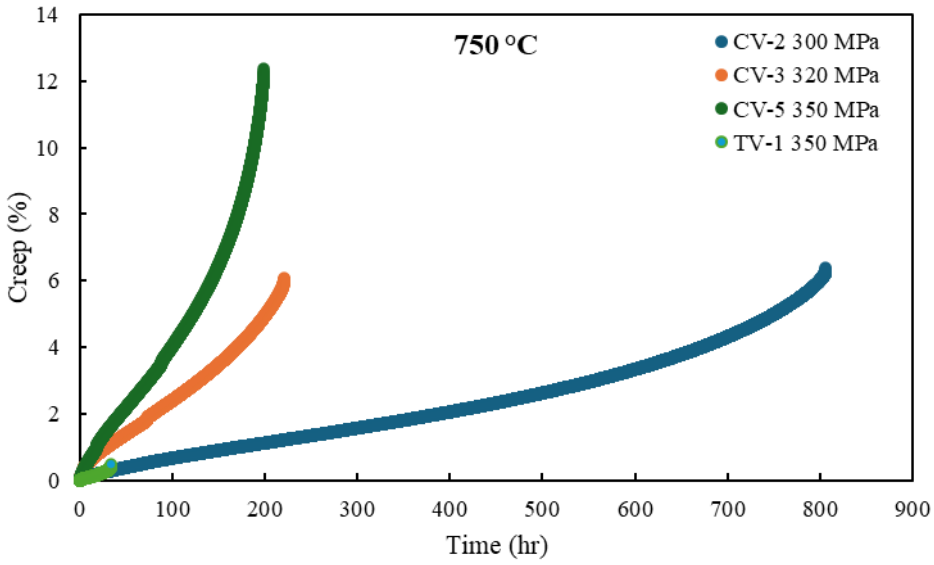

Figure 25. Creep curves from LPBF Haynes 282 tested at INL.

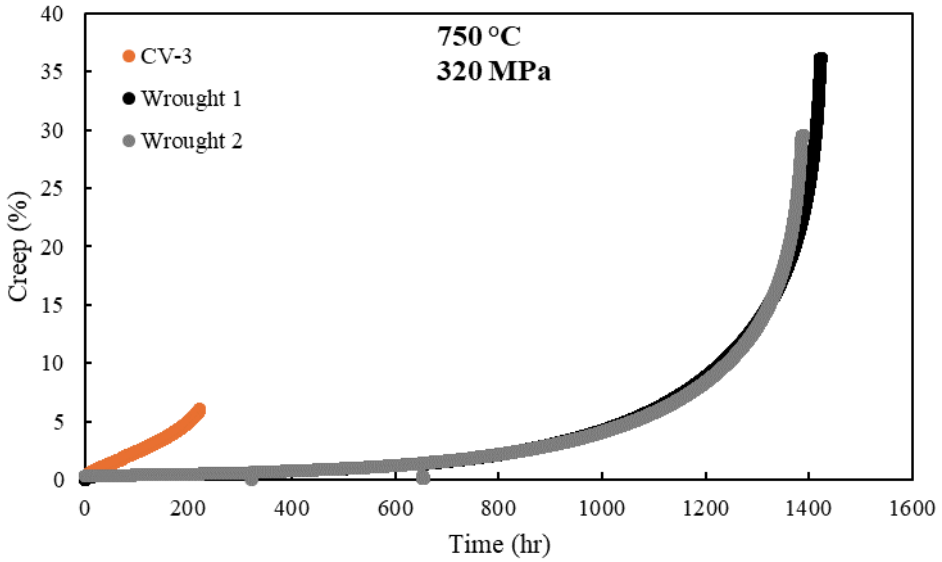

Figure 26. Comparison of LPBF and wrought Haynes 282 tested at INL. Wrought testing was part of a concentrating solar power project. [15]

Table 6. Summary of results from creep testing.

Specimen	Temperature (°C)	Stress (MPa)	Rupture time (hr)	Post-test elongation (%)
CV2	750	300	806	5.97
CV3	750	320	221	5.39
CV5	750	350	199	11.07
TV1	750	350	33	1.89

3.1.5. Cyclic testing

A fatigue and a creep-fatigue test were performed on the LPBF material at conditions that could be compared to the wrought material tested in the solar program. [15] Creep-fatigue is a cyclic test like fatigue, with the inclusion of a hold time each cycle at peak strain. In this case, the hold time was 10 minutes, during which time stress relaxation is allowed to occur. Typically, a significant decrease in cyclic life is observed in creep-fatigue test, as compared to fatigue, due to the interaction between creep and fatigue damage. The results shown in Figure 27 show that the LPBF material, similar to the creep testing, has poorer life when compared to the wrought material for both fatigue and creep fatigue.

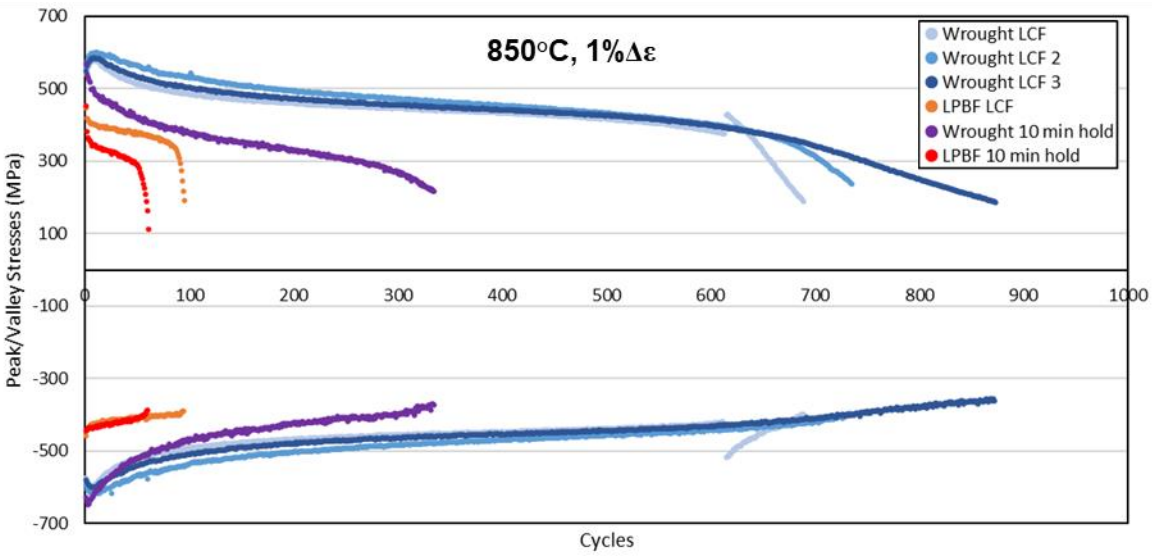

Figure 27. Fatigue curves of LPBF Haynes 282 tested in this program compared to wrought material tested as part of a concentrating solar power project. [15]

3.2. LP-DED

3.2.1. Powder feedstock

SEM images, Figure 28, of HY282 powder feedstock show a nonuniform powder morphology with the presence of nonspherical and amorphous particles. For LP-DED, spherical powder with a size distribution of 45-150 µm is ideal to limit the formation of interlayer porosity. The nonuniform sphericity of the powder increases the chance that interlayer porosity will develop in the LP-DED specimens. The chemical composition analysis for the as-deposited material is shown in Table 7. No significant changes were noted in the elements measured. However, influential elements such as carbon, oxygen, nitrogen, and boron have not been measured but are critical for future analysis.

Table 7. Powder feedstock composition versus the as-deposited LP-DED composition.

	Chemical Composition (wt%)								
	Si	**Al**	**Ni**	**Co**	**Fe**	**Mn**	**Cr**	**Ti**	**Mo**
Powder	0.08	1.52	53.73	9.35	0.215	0.02	16.92	1.95	8.25
As-deposited	0.12	1.49	53.3	9.67	0.21	0.02	17.21	1.99	8.44

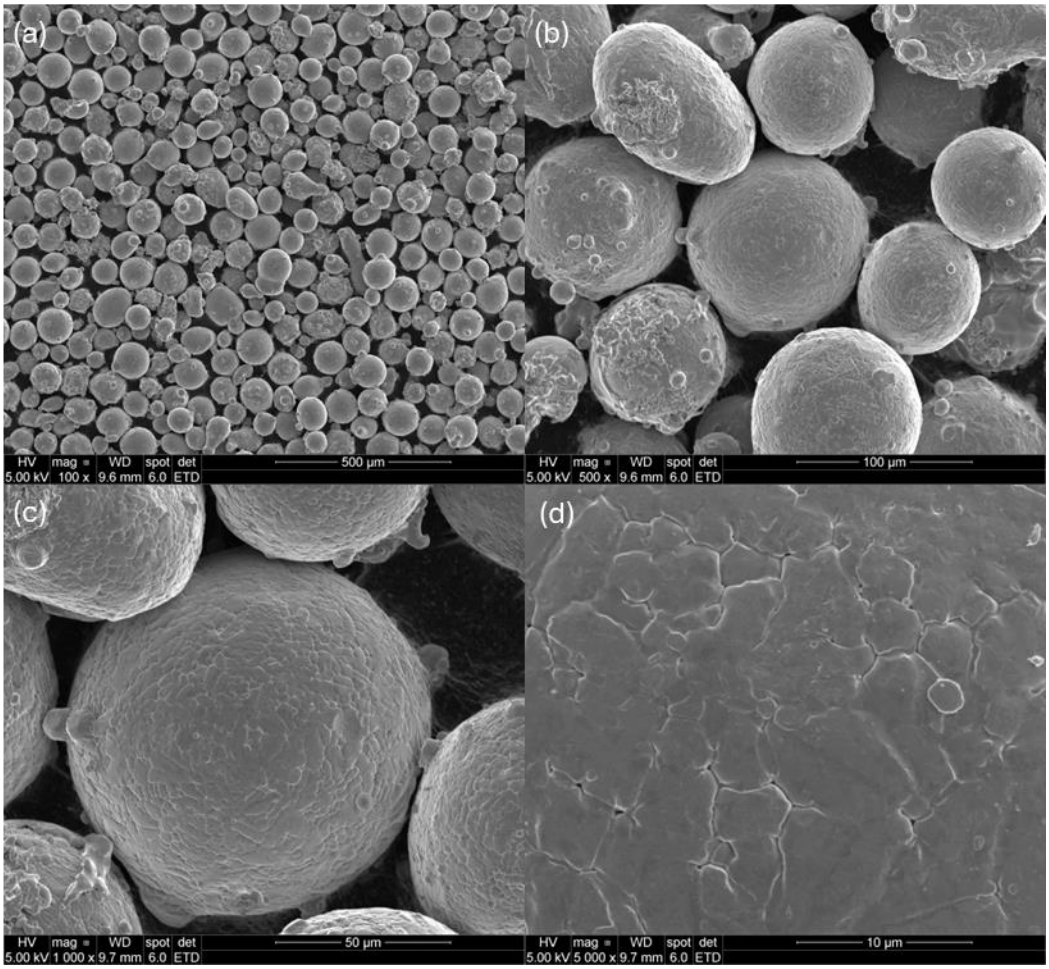

Figure 28. SEM electron backscatter image showing morphology and particle size distribution of Haynes 282 powder feedstock for LP-DED at (a) 100x, (b) 500x, (c) 1000x, and (d) 5000x.

3.2.2. EBSD Analysis

EBSD analysis was performed on the as-deposited, solution annealed, and age hardened conditions as shown in Figure 29 and Figure 30. The as-deposited sample, top images in Figure 29 and Figure 30, show epitaxial grain growth oriented towards the [111] direction, though the number of grains samples is very limited at this point. After annealing at 1180 °C for 1 hour, the center image in Figure 29 and Figure 30, incomplete recrystallization was observed with elongated columnar grains associated with solidification in metal AM processes mixed with equiaxed grains. Annealing twins can also be seen in the material which are known to form during recrystallization in low stacking fault energy materials like Ni-based alloys. [16] Scans after the age hardening at 800 °C for 4 hours are shown in the lower images in Figure 29 and Figure 30.

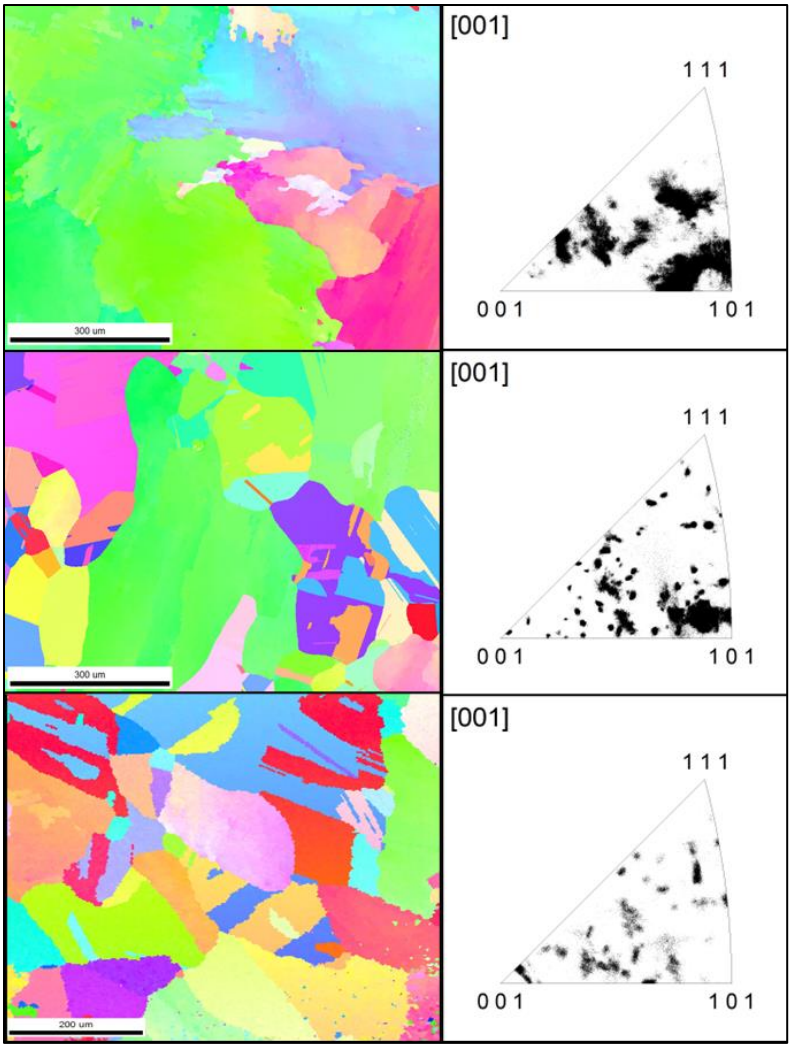

Figure 29. EBSD analysis normal to the build direction of HY282 fabricated by LP-DED in as-deposited (top), solution annealed (center), and age hardened conditions (bottom).

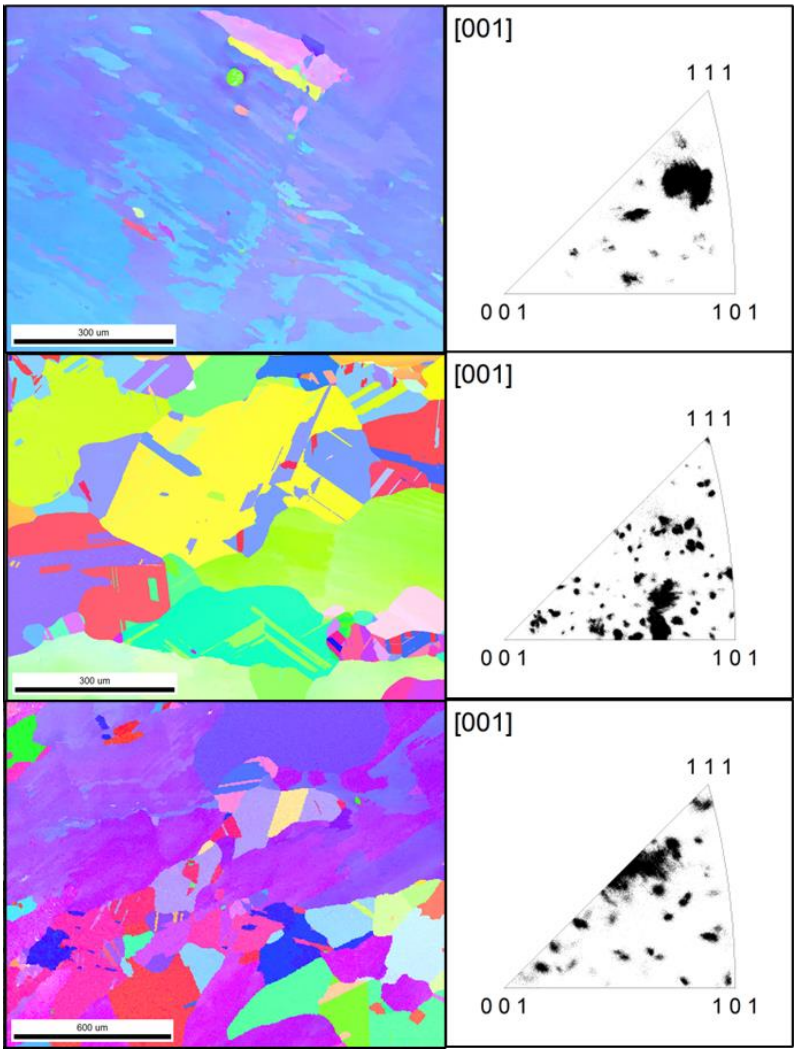

Figure 30. EBSD analysis transverse to the build direction of HY282 fabricated by LP-DED in as-deposited (top), solution annealed (center), and age hardened condition (bottom).

3.2.3. Carbide Evolution

SEM and EDS analysis, Figure 31, shows concentrations of Ti and Mo dispersed through the metal matrix indicating the presence of (Ti, Mo)C carbides in the as deposited and annealed samples. The age hardened sample shows concentrations of Mo, Mn, and Cr along the grain boundaries suggesting the presence of $(Cr, Mn, Mo)_{23}C_6$ carbides with (Ti, Mo)C carbides still present, shown in Figure 32. Cast HY282 shows similar trends for carbide evolution during heat-treatment. [17]

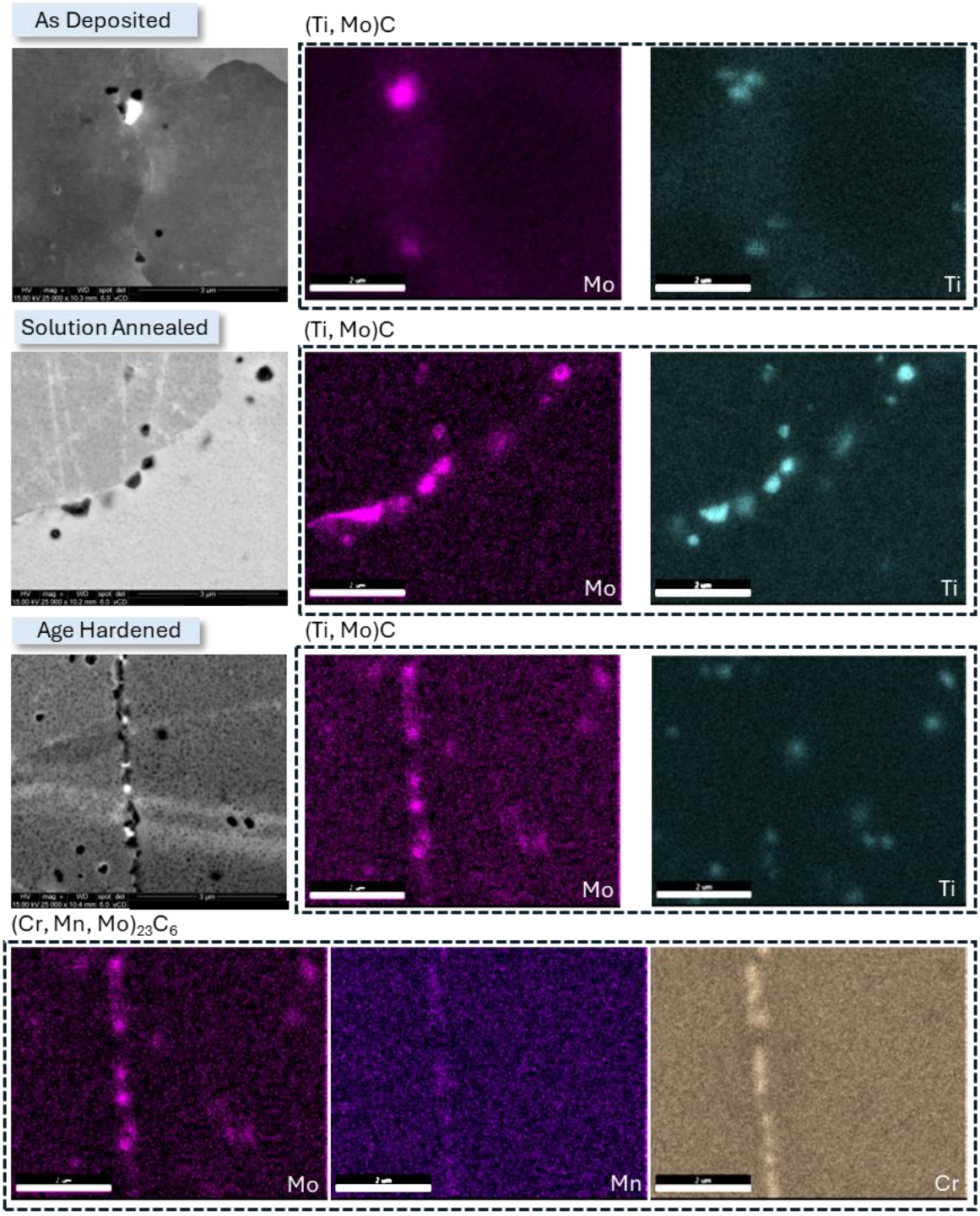

Figure 31. SEM and EDS analysis of the evolution of (Ti, Mo)C and $(Cr, Mn, Mo)_{23}C_6$ carbides during the heat treatment process. Only (Ti, Mo)C is present in the as-deposited and annealed material.

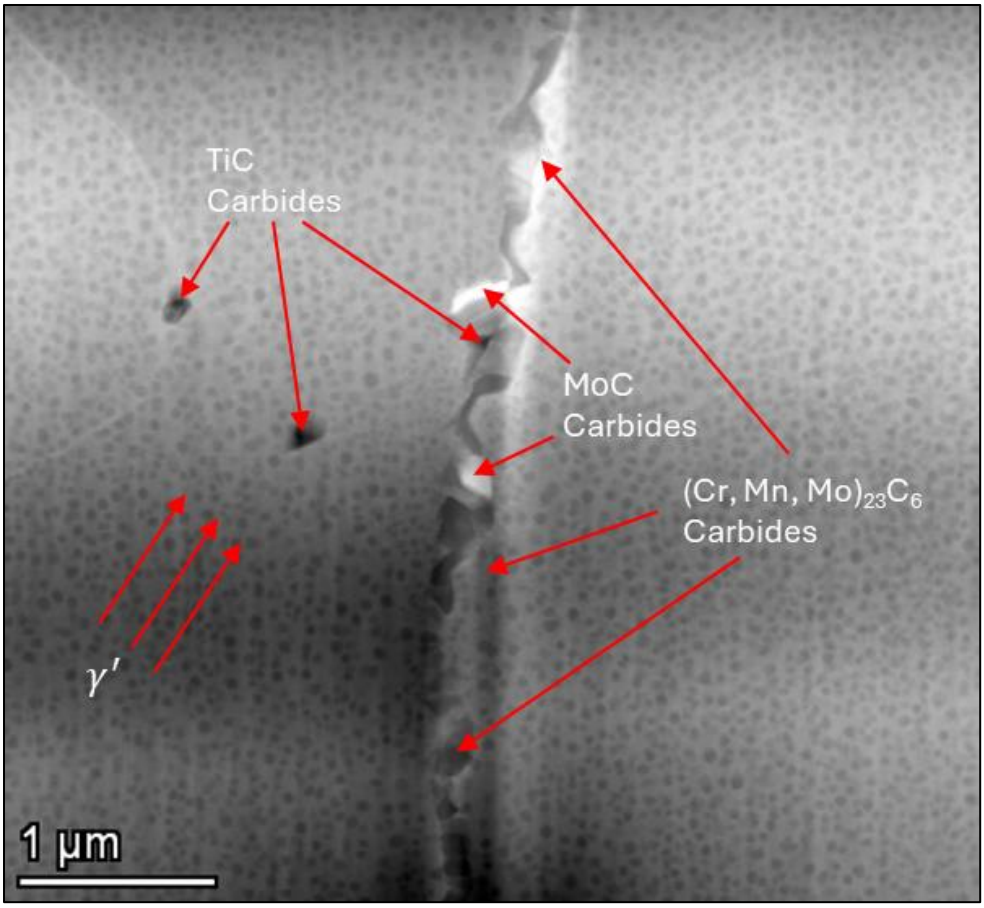

Figure 32. Transmission electron microscope image showing γ' precipitation and discrete carbides along the grain boundary and distributed though out the metal matrix in an age hardened LP-DED HY282 sample.

3.2.4. STEM Analysis

STEM line scans across γ' precipitates, Figure 33, showed an increase in atomic wt% of Ni, Al, and Ti with a decrease in Cr with no notable change in Co or Mo. Scan across a grain boundary showed a significant increase in atomic wt% of Cr with a corresponding decrease in Ni. In addition, there was an increase in Mo with a decrease in Al, Co, and Ti. At approximately 22 nm distance there appears to be γ' precipitates along the grain boundary with a notable increase in Ni, Al, and Ti with a decrease in Cr and Mo. Line scan across a secondary carbide shows a significant increase in Ti and decrease in Ni. There is a slight increase in Mo and decrease in Cr, Co, and Al. STEM EDS, Figure 34, map showing elemental distribution around grain boundary of age hardened HY282 sample fabricated by LP-DED. EDS mapping indicates the presence of $(Cr, Mn, Mo)_{23}C_6$ carbides along the grain boundary and (Ti, Mo)C carbides along the grain boundary and distributed throughout the metal matrix.

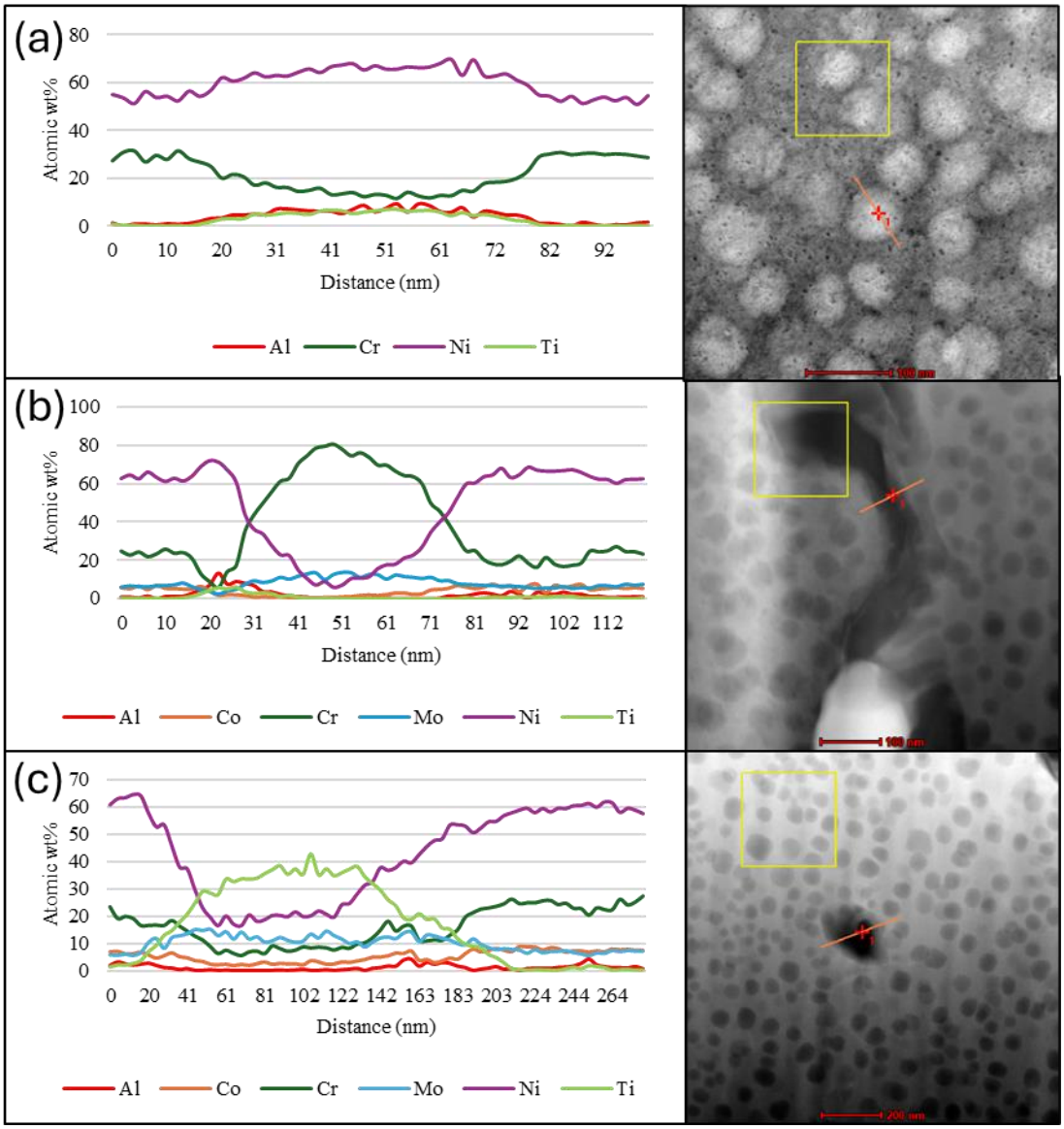

Figure 33. STEM and EDS line scans across (a) γ' precipitates, (b) grain boundary, and (c) secondary TiC carbide.

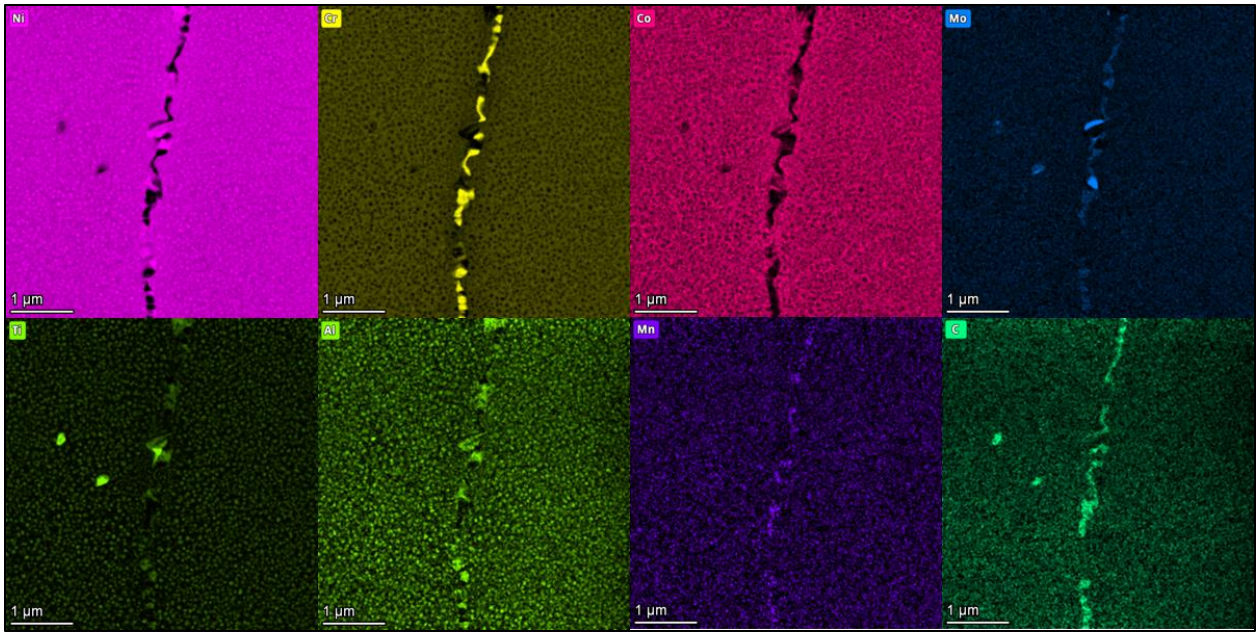

Figure 34. STEM EDS map showing elemental distribution around grain boundary of age hardened HY282 sample fabricated by LP-DED.

3.2.5. Hardness

The hardness values for LP-DED and GMA-DED are shown in Figure 35. The as-built hardness of the LP-DED was nearly 50 $HV_{0.3}$ greater than the as-built wire DED material. After heat treatments, the hardness values are comparable for both materials within the error of plus/minus one standard deviation. The age hardening heat treatment resulted in the highest hardness of nearly 350 $HV_{0.3}$, likely because of the precipitation and finer distribution of γ'. For comparison, the hardness of cast Haynes 282 in the annealed and age hardened condition are reported to be 250 HV and 263 HV, respectively. [18] Hardness levels near 350 HV for aged Haynes 282 in wrought (sheet) form have been observed. [19]

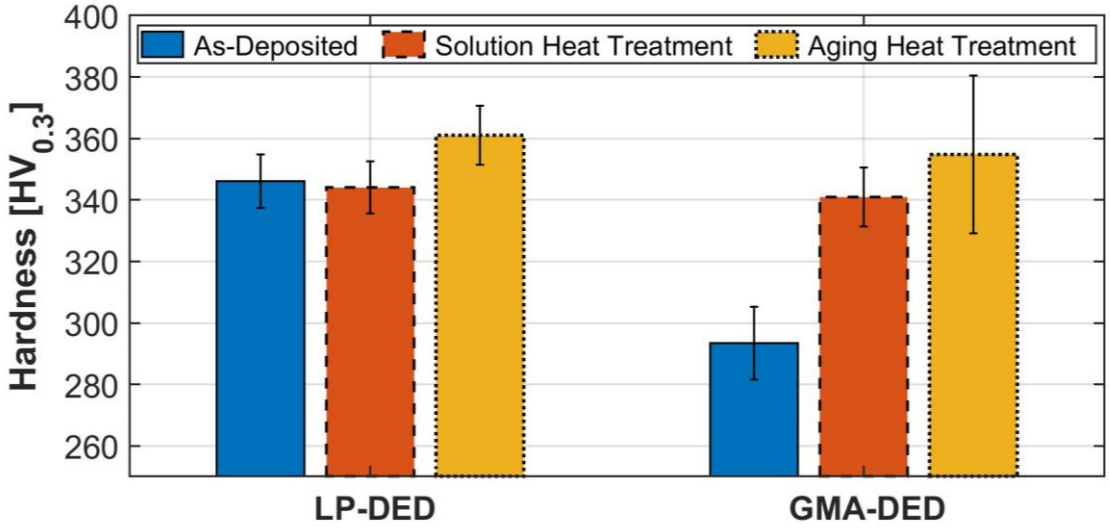

Figure 35. Micro-Vickers Hardness for HY282 LP-DED and GMA-DED.

3.2.6. X-Ray Diffraction

The x-ray diffraction plots of the powder feedstock, as-deposited, and heat-treated HY282 samples are shown in Figure 36. The diffraction peaks in the specimens corresponding to the γ and γ' phases occur at 2Theta = 43.5°, 50.7°, 74.6°, 90.6°, and 96° which correspond to the diffraction of (111), (200), (220), (311), and (222) planes of the γ and γ' phase. Due to the very small lattice parameter variation between γ and γ' the presence of γ/ γ' phase is difficult to differentiate in nickel-based super alloys. [20] MC, M_6C, and $M_{23}C_6$ carbides usually have weak intensities due to the very low volume fraction of carbides and small size, however peaks corresponding to MC carbides occur around 2Theta = 42°, 77.5°, and 96.7° with increasing intensity from as deposited to age hardened. The peak at 2Theta = 54° indicated the presence of the undesirable η phase. Nickel-based superalloys with high Ti/Al ratios commonly show precipitation of the η phase which has an ordered hexagonal $D0_{24}$ structure with a Ni_3Ti stoichiometry and is the equilibrium phase corresponding to the metastable γ'-Ni_3(Al, Ti). [21]

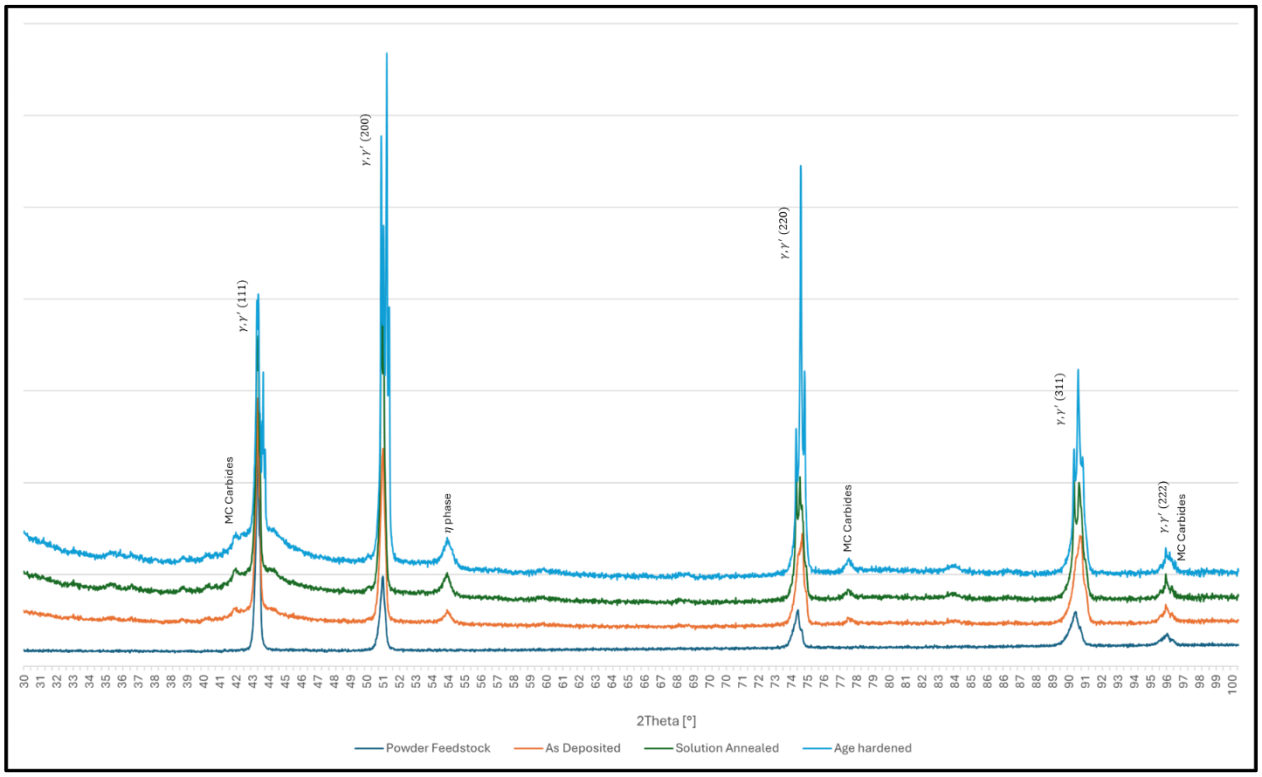

Figure 36. XRD plots of powder, as deposited, solution annealed, and age hardened samples.

3.3. GMA-DED

3.3.1. SEM EDS Analysis

EDS mapping in GMA-DED HY282, Figure 37 through Figure 39, shows concentrations of Ti and Mo distributed throughout the metal matrix and along grain boundaries. These concentrations show the presence of secondary carbides and nitrides. Laves phase present in solution annealed sample, Figure 38, show similar concentrations. Porosity is also present in the solution annealed EDS map, indicated by the absence of Mo, Ti, Al, and C. The age hardened sample, Figure 39, shows concentrations of Cr, Mo, and Mn along the grain boundaries suggesting the presence of (Cr, Mo, Mn)23C6 carbides.

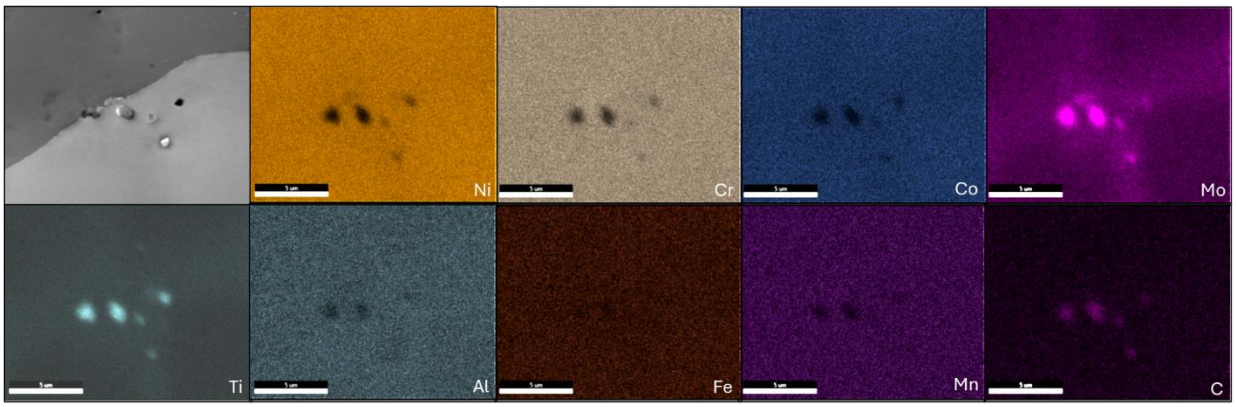

Figure 37. SEM EDS map at 20k x magnification showing elemental distribution around grain boundary of as-deposited HY282 sample fabricated by GMA-DED.

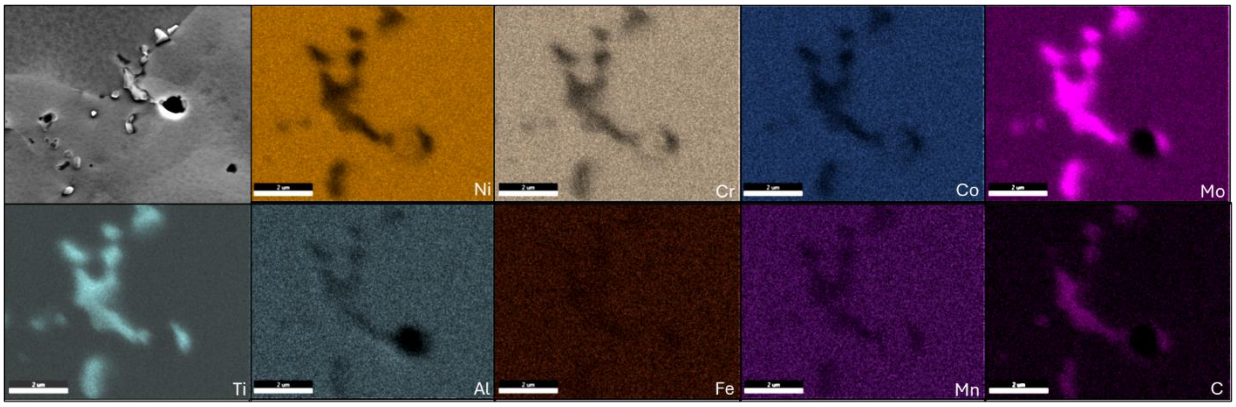

Figure 38. SEM EDS map at 20k x magnification showing elemental distribution around grain boundary of solution annealed HY282 sample fabricated by GMA-DED.

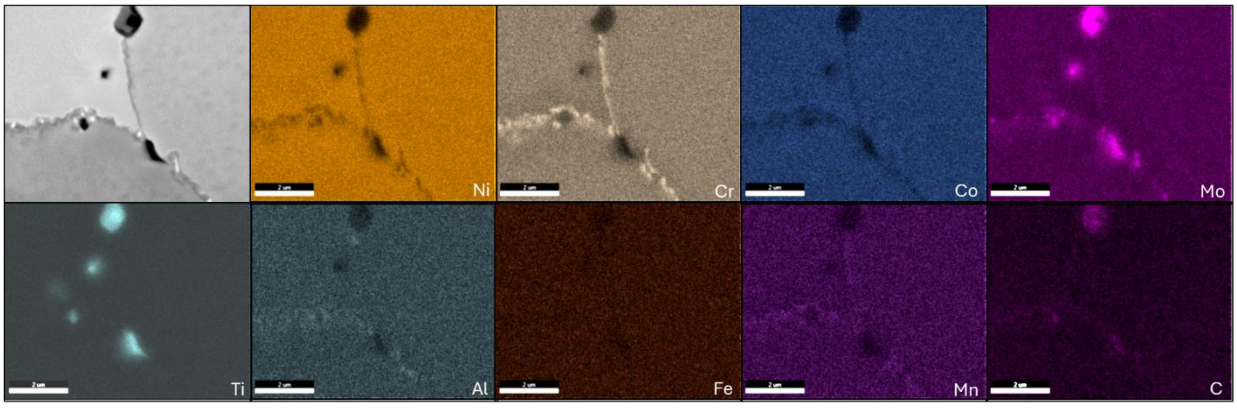

Figure 39. SEM EDS map at 20k x magnification showing elemental distribution around grain boundary of age hardened HY282 sample fabricated by GMA-DED.

Low magnification SEM imaging, Figure 40, of Haynes 282 fabricated by GMA-DED shows incomplete recrystallization during the heat treatment process. The heat treatment performed on samples fabricated by GMA-DED consisted of a solution annealing at 1180 °C for 1 hour followed by air cooling and an age hardening at 800 °C for 4 hours then air cooled. Nitrides, as shown in Figure 41, up to 10 µm diameter are present in Haynes 282 fabricated by GMA-DED in all three states: as-deposited, solution annealed, and age hardened. The Ti in the Haynes 282 will react with nitrogen (N_2) at elevated temperatures when processed in a Ni rich environment.

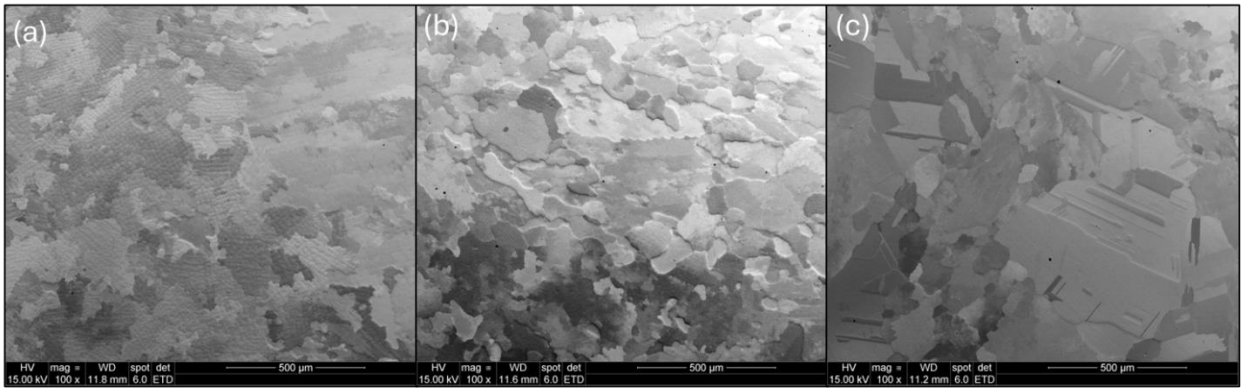

Figure 40. Low magnification SEM imaging showing grain morphology of (a) as-deposited, (b) solution annealed, and (c) age hardened HY282 sample fabricated by GMA-DED.

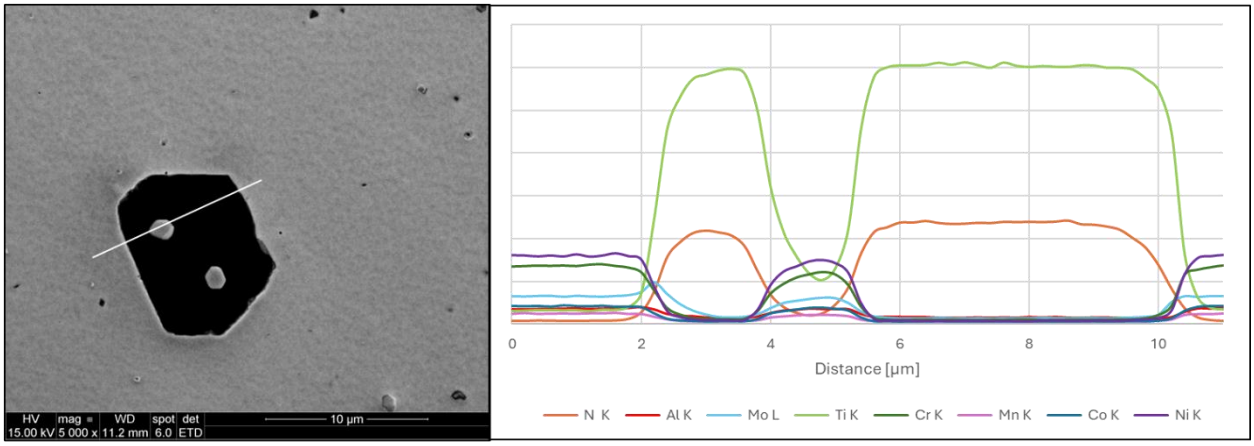

Figure 41. EDS line scan of titanium nitride present in age hardened HY282 fabricated by GMA-DED.

Figure 42 shows EDS line scans across several features present in the age hardened sample. Line 1, across Laves phase shows significant increase in Mo and Ti with corresponding decrease in Ni and Cr. Scan also shows a slight increase in N and C suggesting the presents of both carbides and nitrides. Line 2 across the grain boundary shows a decrease in Ni with an increase in Cr, Mo, and Mn verifying the EDS map results in Figure 39. Line 3 across a secondary phase located at the grain boundary matches the composition change in line 1, suggesting the presents of both carbides and nitrides along the grain boundary.

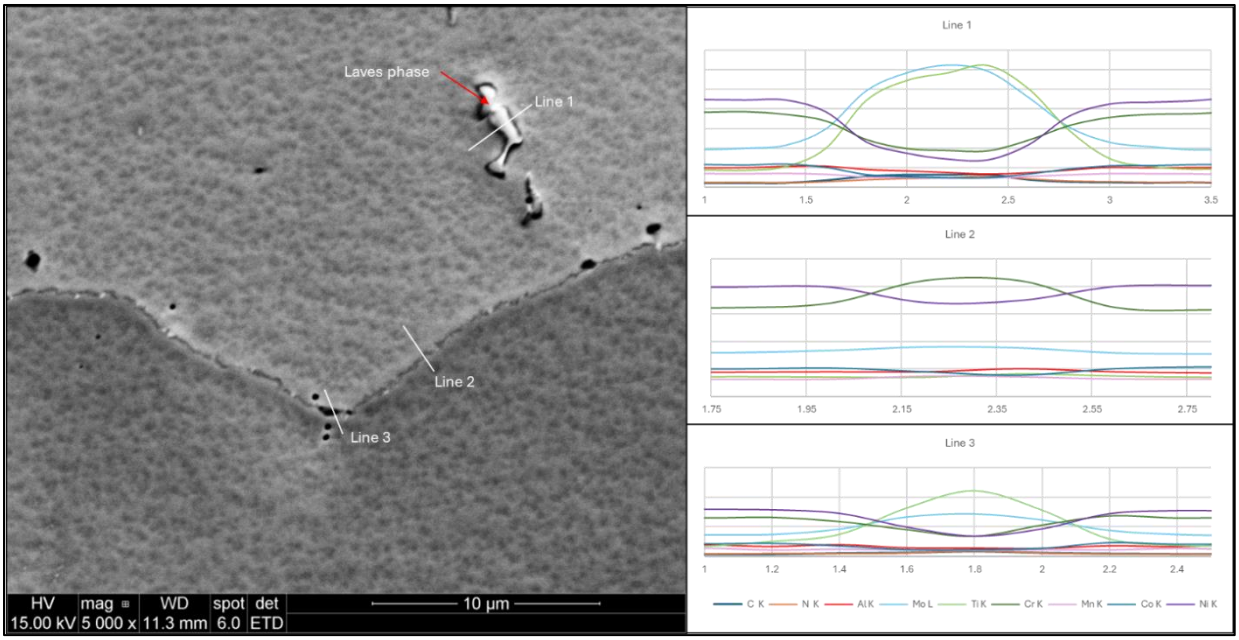

Figure 42. EDS line scans on grain boundary and Laves phase in age hardened HY282 fabricated by GMA-DED.

3.4. Other Alloy Testing

An important area of consideration going into the work for this fiscal year was the need to finish the down-selection to the final molten salt alloy (between Hastelloy N and Haynes 244). While Haynes 244 was found to generally have better mechanical strength, its performance in molten salt was not well studied. [2] Static molten salt testing was performed on both alloys, as well as Alloy 625 and Haynes 282. All four material coupons were made from wrought material. Nickel wire was used to hang the coupons in glassy carbon crucibles, shown in Figure 43. Tests were performed at 750 °C for 1,000 hours. Two separate tests were performed, one in NaCl-$MgCl_2$ salt, and one in FLiNaK salt. Weight loss, summarized in Table 8, was in the following order of more to less severe susceptibility to corrosion: Alloy 625 > Haynes 282 > Haynes 244 ≈ Hastelloy N.

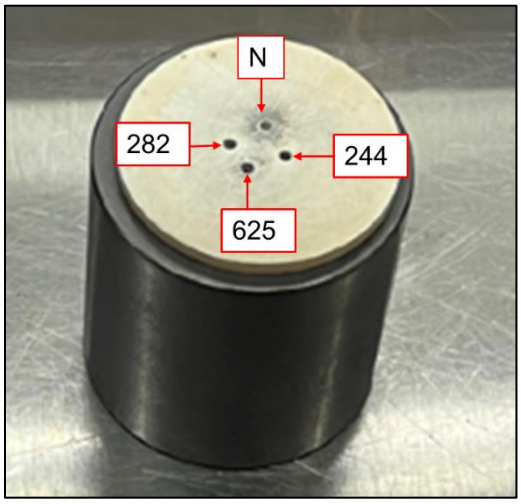

Figure 43. Static molten salt corrosion capsule.

Table 8. Summary of corrosion results from static molten salt experiments.

Test parameters	Specimen ID	Pre-test		Post-test		Weight change ratio (%)
		Mass (g)	Avg Mass (g)	Mass (g)	Avg Mass (g)	
NaCl-MgCl2, 750 °C, 1000 hrs	625-A	0.4570	0.4571	0.4392	0.4392	-3.90
		0.4570		0.4392		
		0.4572		0.4393		
	282-A	0.4929	0.4929	0.4870	0.4870	-1.19
		0.4929		0.4870		
		0.4928		0.4870		
	244-A	0.9197	0.9196	0.9185	0.9185	-0.13
		0.9197		0.9185		
		0.9195		0.9184		
	N-A	0.4909	0.4908	0.4903	0.4903	-0.10
		0.4908		0.4903		
		0.4908		0.4903		
FLiNaK, 750 °C, 1000 hrs	625-B	0.4879	0.4878	0.4283	0.4283	-12.21
		0.4879		0.4283		
		0.4877		0.4282		
	282-B	0.4934	0.4935	0.4782	0.4782	-3.09
		0.4935		0.4782		
		0.4935		0.4783		
	244-B	0.9151	0.9152	0.9131	0.9131	-0.23
		0.9153		0.9131		
		0.9153		0.9131		
	N-B	0.4839	0.4838	0.4825	0.4825	-0.27
		0.4839		0.4825		
		0.4836		0.4825		

4. DISCUSSION AND CONCLUSIONS

There were significant levels of voids observed in the LPBF Haynes 282 material, as seen in Table 4, Figure 4 through Figure 6, and Figure 12 through Figure 17. Discussions with ORNL about the manufacturing process led to the conclusion that many of these pores/voids are formed due to the presence of spatter. Spatter can result from material ejected from melt pool, that is carried by the carrier gas downstream and settling on the powder layer. In the case of the INL build performed at ORNL, the argon carrier gas entered the build from the side of the build plate where specimens FV-5 through FV-8 were located. As a result, FV-1 through FV-4 and the TV specimens are expected to have higher defect densities, as they are downstream on the build plate. In general, this is in agreement with the INL data, though there are variations in data even among specimens within the same columns (same degree downstream) on the build plate.

The different degrees of void densities were shown to have a significant effect on creep testing. While the creep properties of the LPBF Haynes 282 were poor, both in ductility and rupture life, when compared to the wrought material, the difference between CV-5 and TV-1 were extreme. TV-1 was shown in the xCT data (Figure 12) to have a high void density, whereas CV-5 (Figure 17) was quite low. TV-1 had an

extremely poor ductility (~1.9%) and a rupture life of less than 50 hours. CV-5 had a ductility of approximately 11%, and a rupture time of 200 hours. Only limited cyclic testing was performed, which does not allow for a comparison of how initial defects affect the cyclic properties of the LPBF material, however, it does show, similar to the creep properties, that the LPBF material performs significantly more poorly than the wrought material. While none of the LPBF material was fully defect free, several of the specimens had very few defects observed in the xCT scans. The poor life when compared to wrought is not expected to fully be a result of the defects. There appears to be additional issues with the printed microstructure that results in the reduced lives and ductility.

LP-DED samples were fabricated with minimal volumetric defects and no significant compositional change, Table 4. XRD analysis shows the presence of γ, γ', and η phases as well as MC and $M_{23}C_6$ carbides. EDS analysis along grain boundaries in the as-deposited, solution annealed, and age hardened samples confirms the presence of these carbides. Due to their small size MC carbides are not typically detectable in XRD analysis suggesting that the volume fraction present may be higher in the LP-DED samples than in material fabricated by other methods. This could be the cause of the notably higher hardness values for the LP-DED samples at 361 HV compared to 263 HV for cast HY282. EBSD analysis shows incomplete recrystallization during the heat treatment process suggesting that alternative processes should be explored for HY282 fabricated by LP-DED. The GMA-DED samples also show incomplete recrystallization during the heat treatment process. A high volume of secondary carbide and nitride phases are indicated in SEM and EDS analysis. SEM images of heat-treated sample show γ' precipitates and the presence of Laves phases and spherical porosity from gas entrapment. Additional characterization work is still being conducted on samples fabricated by GMA-DED. Cyclic and creep testing is planned for material from both DED processes.

The corrosion results show that Haynes 244 performed well in molten salt, with a similar weight percent drop as Hastelloy N. Given the improved mechanical properties of Haynes 244, and its greater commercially available than Hastelloy N which was a specialty alloy developed specifically for nuclear, it is recommended that Haynes 244 be considered as the final alloy down selected for use in molten salt environments.

This work has shown that there are challenges with printing 282. Even low void densities in the material do not result in acceptable high temperature mechanical properties like creep. Further work is needed to fully understand what level of voids/discontinuities can be tolerated, what constitutes a defect for each AM process, and the microstructures that will be generated within these build/process regimes. Otherwise, the resulting material properties will continue to show large decreases in expected material lifetimes and ductility. INL manufactured Haynes 282 using two different DED processes and feedstocks. The results of characterization on these alloys have been presented in this report. Mechanical test specimens are continuing to be prepared and testing will be performed to further investigate the properties of the material manufactured through the DED processes. This may provide additional insight into the AM effects on the high temperature material properties, such as the differences between the LPBF and DED material, as well as between the LP-DED and the GMA-DED. Finally, the preliminary corrosion results showed similar molten salt resistance for Haynes 244 as was observed for Hastelloy N. Therefore, Haynes 244 is recommended to the AMMT program as being the third nickel alloy of interest and merits further study.

5. REFERENCES

[1] M. D. McMurtrey, M. J. Moorehead and M. D. Mulholland, "INL/RPT-23-73948 Evaluation of Nickel Alloys, Manufactured through Powder Bed Fusion, for Application for Advanced Nuclear Reactors," 2023.

[2] S. Dryepondt and e. al., "ORNL/TM-2023/3108 Prioritization of Existing Reactor Mateirals," 2023.

[3] L. M. Pike, "Development of a fabricable gamma-prime strengthened superalloy," in *Superalloys 2008*, R. Reed, K. A. Green, P. Caron, T. P. Gabb, M. Fahrmann, E. Huron and S. A. Woodard, Eds., 2008, pp. 191-200.

[4] R. Viswanathan, J. Shingledecker and R. Purgert, "Evaluating Materials Technology for Advanced Ultrasupercritical Coal-Fired Plants," *Power*, vol. 154, pp. 41-45, 2010.

[5] P. D. Jablonski, J. A. Hawk, C. J. Cowen and P. J. Maziasz, "Processing of Advanced Cast Alloys for A-USC Steam Turbine Applications," *JOM*, vol. 64, pp. 271-279, 2012.

[6] C. Shen, "Modeling Creep-Fatigue-Environment Interactions in Steam Turbine Rotor Materials for Advanced Ultra-Supercritical Coal Power Plants," 2014.

[7] B. A. Pint, H. Wang, C. S. Hawkins and K. A. Unocic, "ORNL/TM-2020/1548 Technical Qualification of New Mateirals for High Efficiency Coal-Fired Boilers and Other Advanced FE Concepts: Haynes 282 ASME Boiler and Pressure Vessel Code Case," 2020.

[8] R. Rajan, "Developing an Ultra-Compact, Topology-Optimized Heat Exchanger using Additive Manufacturing," 2022.

[9] C. Magnin, Z. Islam, M. Elbakhshwan, A. Brittan, D. J. Thoma and M. H. Anderson, "The Performance of Additively Manufactured Haynes 282 in Supercritical CO2," *Materails Science & Engineering A*, vol. 841, p. 143007, 2022.

[10] A. S. Shaikh, F. Schulz, K. Minet-Lallemand and E. Hryh, "Microstructure and Mechanical Properties of Haynes 282 Superalloy Produced by Laser Powder Bed Fusion," *Materials Today Communications*, vol. 26, p. 102038, 2021.

[11] Z. Islam, A. Kumar, A. B. Rankouhi, C. Magnin, M. H. Anderson, F. E. Pfefferkorn and D. J. and Thoma, "A Hgih-Throughput Method to Define Additive Manufacturing Process Parameters: Application to Haynes 282," *Metallurgical and Materials Transactions A*, vol. 53, pp. 250-263, 2022.

[12] J. Boswell, J. Jones, N. Barnard, D. Clark, M. Whittaker and R. Lancaster, "The Effects of Energy Density and Heat Treatment on the Microstructure and Mechanical Properties of Laser Additive Manufactured Haynes 282," *Materials & Design*, vol. 205, p. 109725, 2021.

[13] K. Christofidou, H. T. Pang, W. Li, Y. Pardhi, C. N. Jones, N. G. Jones and H. J. Stone, "Microstructural Control and Optimization of Haynes 282 Manufactured through Laser Powder Bed Fusion," in *SuperAlloys 202*, S. Tin, M. Hardy, J. Clews, J. Cormier, Q. Feng, J. Marcin, C. O'Brien and A. Suzuki, Eds., 2020, pp. 1014-1023.

[14] American Welding Soceity, *A5. 14/A5. 14m:2024 Specification for Nickel and Nickel-Alloy Bare Welding Electrodes and Rods*, 2024.

[15] M. C. Messner, B. Barua and M. D. McMurtrey, "ANL-22/29 srlife: A Fast Tool for High Temperatuer Receiver Design and Analysis," 2022.

[16] N. Dudova, A. Belyakov, T. Sakai and R. Kaibyshev, "Dynamic Recrystallization Mechanisms Operating in a Ni-20% Cr Alloy under Hot-to-Warm Working," *Acta Materialia*, vol. 58, no. 10, pp. 3624-3632, 2010.

[17] Y. Yang, R. C. Thomson, R. M. Leese and S. Roberts, "Microstructural Evolution in Case Haynes 282 for Application in Advanced Power Plants," *Advances in Materials*, vol. 84666, pp. 143-154, 2013.

[18] A. Polkowska, W. Polkowski, M. Warmuzek, N. Cieśla, G. Włoch, D. Zasada and R. M. Purgert, "Microstructure and Hardness Evolution in Haynes 282 Nickel-based Superalloy during Multi-Variant Aging Heat Treatment," *Journal of Mateirals Engineering and Performance*, vol. 28, pp. 3844-3851, 2019.

[19] S. Haas, J. Andersson, M. Fisk, J.-S. Park and U. Lienert, "Correlation of Precipitate Evolution with Vickers Hardness in Haynes 282 Superally: In-situ High-energy SAXS/WAXS Investigation," *Materials Science and Engineering A,* vol. 711, pp. 250-258, 2018.

[20] A. Ramakrishnan and G. P. Dinda, "Microstructure and Mechanical Properties of Direct Laser Metal Deposited Haynes 282 Superalloy," *Materials Science and Engineering A,* vol. 748, pp. 347-356, 2019.

[21] K. Hou, M. Ou, W. Xing, G. Ma, X. Hao, M. Wang and Y. Ma, "The Formation of η-Ni3Ti Phase Microstructure in a Cast Nickel-based Superalloy with High Ti/Al Ratio," *Journal of Materials Research and Technology,* vol. 29, pp. 764-778, 2024.

[22] K. A. Unocic, D. Shin, X. Sang, E. Cakmak and P. F. Tortorelli, "Single-Step Aging Treatment for a Precipitation0Strengthened Ni-Based Alloy and its Influence on High-Temperature Mechanical Behavior," *Scripta Materialia,* vol. 162, pp. 416-420, 2019.

[23] M. Romedenne, P. Stack, R. Pillai and S. Dryepondt, "Isothermal and Cyclic Oxidation of Haynes 282 Processed by Electron Beam Melting (EBM) and Laser Powder Bed Fusion (LPBF) in Dry Air at 800 and 950 degrees C," *JOM,* vol. 74, pp. 1707-1718, 2022.

[24] L. Tang, R. Zhou, Y. Guo, B. Wang and S. Hou, "Oxidation Behavior of Haynes 282 in Steam at 750 C," *8th International Symposium on Superalloy 718 and Derivatives,* pp. 863-871, 2014.

Page intentionally left blank